

# Enabling pure CO<sub>2</sub> reduction on Ni{Cu}<sub>x</sub>-YSZ electrode via an oxide-mediated mechanism

Vipin Kamboj, Soham Raychowdhury, Chinmoy Ranjan\*

Department of Inorganic and Physical Chemistry, Indian Institute of Science, Bengaluru 560012, India



## ARTICLE INFO

### Keywords:

Solid oxide electrolysis  
CO<sub>2</sub> reduction  
Operando Raman spectroscopy  
Electrocatalysis

## ABSTRACT

Ni-YSZ-based electrodes are well-known as CO<sub>2</sub> reduction cathodes. These electrodes require the presence of safe gases such as H<sub>2</sub> or CO in the CO<sub>2</sub> inlet stream, adding substantial complexity to the devices. Various reasons such as electrode oxidation and coking have been historically attributed to electrode failure in pure CO<sub>2</sub> streams. Using operando Raman spectroscopy and online mass spectroscopy, we have shown that Ni-YSZ electrodes can, in fact, be operated within certain limits. Our measurements reveal that under operation conditions, Ni-YSZ, in fact, oxidizes to NiO<sub>x</sub>-YSZ. However, it is this oxide that enables the CO<sub>2</sub> reduction via a surface oxygen and oxygen vacancy-mediated mechanism. The deactivation of the electrode coincides with strongly reducing conditions where the NiO<sub>x</sub> is reduced to metallic Ni. Cu-infiltration into Ni-YSZ architecture was demonstrated to mitigate the deactivation issue by modulating the Ni-O-Ni bond strengths and forming a more stable oxide on Ni. This oxide with higher stability to reduction continued to carry out CO<sub>2</sub> reduction under strongly reducing conditions. The new electrode also demonstrated improved kinetics and stability against carbon deposition via Boudouard reaction.

## 1. Introduction

Global targets of CO<sub>2</sub> reduction require aggressive mitigation of CO<sub>2</sub> production and increased capture [1]. Capturing CO<sub>2</sub> from various sources (including air) and converting it into synthetic fuel using green energy is an excellent way of making the fuel usage cycle carbon neutral [2–4].

High-temperature electrochemical reduction of CO<sub>2</sub> within a solid oxide electrolysis cell (SOEC) is an attractive approach allowing for cost-effective and energy-efficient production of CO [5,6]. The electrochemical conversion of CO<sub>2</sub> to CO is relatively energy efficient with 100% faradaic efficiency and greater than 90% energy efficiency. The efficiency losses increase significantly when higher hydrocarbons are targeted. Creation of heavily reduced products such as CH<sub>4</sub>, requires multiple electron and proton transfer steps (8e<sup>-</sup> and 8 H<sup>+</sup>). Such multi-step electrochemical reactions result in high energy losses owing to slower kinetics. CO production from CO<sub>2</sub> is a 4e<sup>-</sup> process and thus kinetically easier. Ideally, CO produced from renewable electricity can be easily coupled with the well-known Fischer Tropsch process, resulting in energy-efficient production of higher synthetic hydrocarbons (Fig. 1) [7–9]. SOECs have the advantages of excellent kinetics along

with selectivity towards the products and are more electrical energy-efficient due to the high operating temperature (~ 800 °C) which reduces cell voltage [10–12].

CO<sub>2</sub> electrolysis is carried out on a membrane electrode assembly comprising a CO<sub>2</sub>-reducing cathode, a solid oxide electrolyte, and an oxygen-evolving anode. Nickel on yttria-stabilized zirconia cermet (Ni-YSZ) serves as the popular choice for the cathode. Perovskites such as (La<sub>0.8</sub>Sr<sub>0.2</sub>)<sub>0.95</sub>MnO<sub>3-x</sub> (LSM-YSZ) and YSZ serve as typical choices for oxygen-evolving anode and electrolyte respectively [6,13–18].

Besides Ni-YSZ, several electrode materials have been tested as cathodes. These include perovskites such as La<sub>0.35</sub>Sr<sub>0.65</sub>TiO<sub>3-x</sub>, Sr<sub>2</sub>FeMo<sub>0.5</sub>O<sub>6-x</sub>, (La<sub>0.75</sub>Sr<sub>0.25</sub>)<sub>0.95</sub>Cr<sub>0.5</sub>Mn<sub>0.5</sub>O<sub>3-x</sub>, La<sub>0.2</sub>Sr<sub>0.8</sub>TiO<sub>3-x</sub>, La<sub>0.75</sub>Sr<sub>0.25</sub>Cr<sub>0.5</sub>Mn<sub>0.5</sub>O<sub>3-x</sub> and CeO<sub>2-x</sub> [12,19–29]. They have the advantage over Ni-YSZ in terms of high ionic and electronic conductivity, better redox stability, and resistance to carbon deposition and sulphur poisoning. However, the poor catalytic activity of perovskites compared to Ni-YSZ makes the latter a preferred material [30–32]. Due to its popularity as a SOFC anode, Ni-YSZ has been well-studied and known in the industry. Well-established manufacturing processes leverage its good electrical, catalytic, and mechanical characteristics to create efficient membrane electrode assembly (MEA) architectures.

\* Corresponding author.

E-mail address: [ranjan@iisc.ac.in](mailto:ranjan@iisc.ac.in) (C. Ranjan).

Anode-supported SOFC based on Ni-YSZ are well known for mechanical stability and high efficiency in fuel cells as they enable very thin electrolyte layers. Ni-YSZ is a well-established anode for the SOFC-H<sub>2</sub> fuel cell [33,34]. But when in the context of CO<sub>2</sub> electrolysis, challenges remain [9,35]. Ni tends to easily oxidise in pure CO<sub>2</sub> environments and thus it is a common practice to use safe gases such as H<sub>2</sub> and/or CO alongside CO<sub>2</sub> in the reaction that can maintain a sufficiently reducing atmosphere at the electrode to maintain metallic Ni sites and carry out CO<sub>2</sub> electrolysis. Addition of gases such as H<sub>2</sub> or CO results in additional complexity. Besides this, Ni remains an excellent catalyst for the Boudouard reaction {2CO → C + CO<sub>2</sub>}, allowing for alternate paths for electrode failure [9,36–38]. Owing to additional complexity from safe gases such as H<sub>2</sub> (and/or CO) and dependence on the availability (rather lack of availability) of H<sub>2</sub> infrastructure, a cathode catalyst that can directly convert a pure CO<sub>2</sub> stream into CO with a sustained performance would be of high value. We believe that rather than starting from scratch, there is merit in altering the existing Ni-YSZ based cathode architecture to achieve our electrocatalytic goals. It can reduce the significant time and effort involved in translation to large-scale devices as it can leverage the current manufacturing and process supply chains.

In the context of Ni-YSZ, originally, Bidrawn et al. discussed the possible challenges of using Ni-YSZ electrode in pure CO<sub>2</sub> stream in their 2008 paper [9]. Implicit in the discussion by Bidrawn et al. is the assumption that one needs metallic-Ni sites to carry out CO<sub>2</sub> electrolysis. [9] Their experimental study, however did not focus on Ni-YSZ but on a perovskite La<sub>0.8</sub>Sr<sub>0.2</sub>Cr<sub>0.5</sub>Mn<sub>0.5</sub>O<sub>3</sub> as the CO<sub>2</sub> reduction cathode. The assumption that metallic Ni sites are needed for CO<sub>2</sub> electrolysis has been so pervasive that later studies have only tested Ni-YSZ electrodes within safe environments such as streams containing CO or H<sub>2</sub> alongside CO<sub>2</sub> or have used modified Ni electrodes [6,39–44].

There has been no experiment that directly implicated oxidation of Ni for electrode failure in CO<sub>2</sub> electrolysis. Ni-YSZ electrode, in fact, has not been investigated in much detail in pure CO<sub>2</sub> streams. Preliminary studies reported in this field provide a somewhat inconsistent and contradictory picture of what happens to Ni-YSZ in pure CO<sub>2</sub> streams [13, 35,45,46]. Dong et al. indicated that the electrode failed, Song et al. claimed that the electrode worked and Chen et al. claimed that Ni-YSZ works under low bias. These studies lack direct observation of the ongoings of Ni-YSZ in pure CO<sub>2</sub> streams due to the use of ex-situ characterization.

We investigated Ni-YSZ under limiting conditions. We repeatedly created conditions of optimal electrode performance and catastrophic failure. In our study, we have shown that Ni-YSZ works under low bias, but upon increasing the bias beyond a critical threshold the electrode catastrophically deactivates. Upon infiltrating the electrode with Cu, the electrode failure is mitigated, and sustained performance could be achieved even at high bias. We have investigated this contrasting performance of these two electrodes (Ni-YSZ, Ni{Cu}<sub>x</sub>-YSZ) using operando spectroscopic techniques. We have used online mass spectrometry and operando Raman spectroscopy to directly correlate catalyst structure with electrochemical activity and CO production in both these electrodes. We have additionally used a thin (~10 μm) cathode so that both active performance and deactivation phenomena can be created. The pre-treatment steps leading to active catalyst formation have also been characterized. Our results, for the first time, allow a direct spectroscopic evaluation of the Ni-YSZ catalyst deactivation process and its mitigation within the Cu-infiltrated counterpart. In our studies, contrary to the prevalent notion, we have shown that within the Ni-YSZ catalyst, the active material for CO<sub>2</sub> reduction is a type of nickel oxide (NiO<sub>x</sub>), the same which develops under open circuit conditions in the presence of CO<sub>2</sub>. We have shown that a progressive regime of cathodic current application results in reduction of this oxide. At high enough negative bias, the oxide layer is completely reduced co-inciding with catalyst deactivation and stoppage in CO production. On the other hand, the Cu-infiltrated catalyst is less reducible and allows the formation of a “stable” oxide layer which does not get completely removed even under strong bias. This oxide layer can engage with CO<sub>2</sub> molecule and reduce it to CO. We have shown that Ni{Cu}<sub>x</sub>-YSZ catalyst also suppresses the Boudouard reaction. In our study Ni-O-Ni bond strength emerges as the primary descriptor of stability in pure CO<sub>2</sub> streams. Cu doping, in fact, increases the Ni-O-Ni bond strength making the catalyst more stable to reduction.

Mechanistically, oxide electrodes have been better analysed for pure CO<sub>2</sub> electrolysis. Ye et al. have reported CO<sub>2</sub> electrolysis on (La, Sr) TiO<sub>3-x</sub> cathodes and shown that “carbonate type” species can form upon CO<sub>2</sub> adsorption on the cathode using in situ infrared spectroscopy in combination with temperature programmed desorption experiments [18,47]. Similar observations have also been reported by Opitz et al. using in situ near ambient pressure (~7 mbar) XPS [48]. Wang et al. have shown that electrodes that result in in-situ exsolution of nanoscale

## CO<sub>2</sub> electrolysis using Solid Oxide Electrolyzers

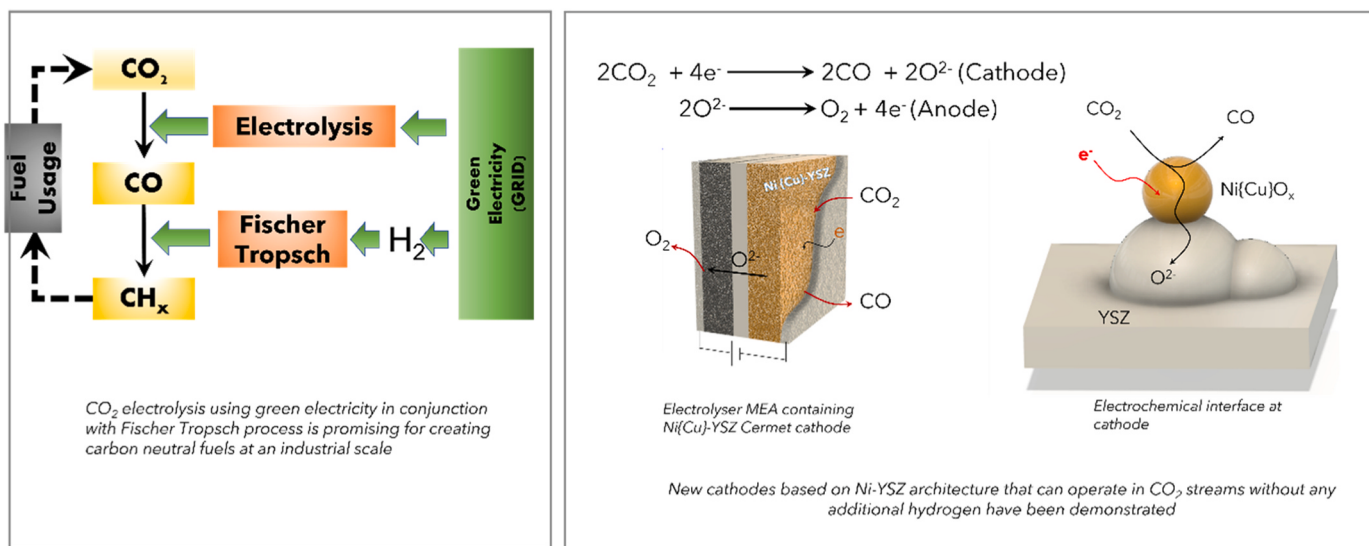


**Fig. 1. : CO<sub>2</sub> neutral fuel cycle.** Green electricity can be channeled into energetic fuels using a combination of CO<sub>2</sub> electrolysis and Fischer Tropsch reaction. This study has demonstrated the CO<sub>2</sub> electrolysis without using additional H<sub>2</sub> with copper-impregnated Ni{Cu}<sub>x</sub>-YSZ electrodes.

metal/metal oxide interfaces perform well in CO<sub>2</sub> reduction [28]. Feng et al. have studied pure CO<sub>2</sub> electrolysis on Sm-doped CeO<sub>2-x</sub> electrode using near ambient pressure XPS and suggested a “carbonate type” mechanism mediated by vacancies on ceria [49].

From our studies, we have argued that CO<sub>2</sub> reduction on the active catalyst material NiO<sub>x</sub> follows an oxide-mediated mechanism where surface oxygen and vacancies mediate a carbonate-type intermediate as proposed in LSM and CeO<sub>2-x</sub> type cathodes. We have proposed that the

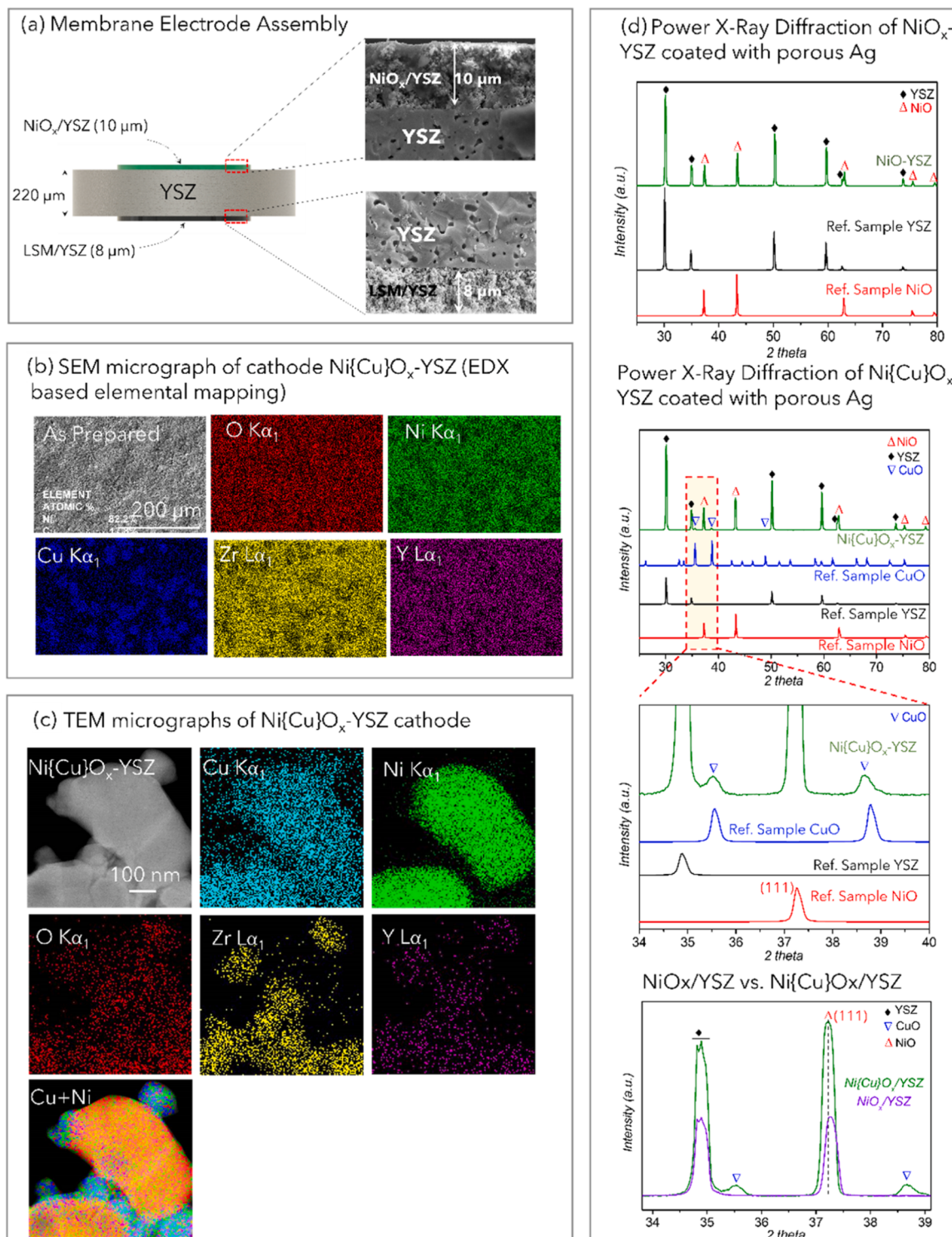


**Fig. 2.** : The cathode (NiO-YSZ, Ni{Cu}O<sub>x</sub>-YSZ) was evaluated post-Cu impregnation and annealing step. The electrodes shown have not been reduced under hydrogen. (a) Membrane electrode assembly used for the studies. The interfaces of the cathode (NiO/YSZ) and anode (LSM/YSZ) with electrolyte (YSZ) are shown. (b) SEM images of the NiO<sub>x</sub>-YSZ/LSM-YSZ cell cross-section are shown. The average composition of Cu was found to be  $\sim 20 \pm 3\%$  and that of Ni to be  $\sim 80 \pm 3\%$  using EDX (c). The STEM images of Ni{Cu}O<sub>x</sub>-YSZ were collected in HAADF mode. Elemental mapping was performed using EDX. (d) The PXRD patterns for NiO-YSZ and Ni{Cu}O<sub>x</sub>-YSZ electrodes are shown. The reference samples have been obtained from ICDD (International Center for Diffraction Data). The JCPDS numbers have been reported in the supporting section ([Supplementary note 2](#)).

active material is likely to be a dynamically stable oxide that has sufficient vacancies and stability to interact with the CO<sub>2</sub> molecule and transfer the O<sup>2-</sup> ion to the electrolyte. Our results indicate that it's possible to develop new catalysts for pure CO<sub>2</sub> reduction using earth-abundant metals such as Ni and Cu.

## 2. Preparation of the Membrane Electrode Assembly (MEA)

The MEA was prepared by screen printing NiO-YSZ (66:34) and LSM-YSZ (50:50) inks on the sides of YSZ solid electrolyte (220 μm thickness, 25 mm diameter) forming the cathode and anode respectively. All the above materials were obtained from Fuel Cell Materials. The MEA was air-dried at 30 °C for 8 h. Subsequently, it was heated (air, heating rate (2 °C/min)) up to 1050 °C and annealed for 3 h. The cell was allowed to furnace cool to room temperature. For electrodes modified with Cu (Ni{Cu}<sub>x</sub>-YSZ), a 20 μl precursor solution of 0.2 M Cu(NO<sub>3</sub>)<sub>2</sub>.3 H<sub>2</sub>O (Thomas Baker) was infiltrated into the NiO-YSZ electrode and dried at 30 °C for 12 hrs to allow impregnation of precursor solution into the electrode. It was followed by sintering at 800 °C for an hour. After furnace cooling, current collectors (porous Ag paste, Fuel Cell Materials) were screen-printed on both sides of the pellet. The MEA was dried at 30 °C for 6 hrs followed by sintering at 500 °C for 1 hr (heating rate 5 °C/min). All the measurements were carried out in a 3-electrode geometry with the concentric Ag reference electrode screen printed on the anode side around the LSM-YSZ electrode, as shown in Fig. S1.

The electrode geometry used is similar to that suggested by Rutman et al. which averages out the effects of WE-CE misalignment for planar electrode geometries [50]. Thereafter, the cell was mounted on a stainless steel (SS) reactor. The gas flow was monitored using a mass flow controller. The cell outlet was connected to a mass spectrometer (Hiden HPR-40) for online gas analysis. Electrochemical studies were carried out using Autolab PGSTAT 30. Operando Raman studies were performed using InVia confocal Raman Microscope (Renishaw) using a 532 nm laser. For operando studies at high temperature, a 2-chamber operando cell was constructed in-house. Further characterization details are provided in the [supporting information](#) (Supplementary Note 1).

### 2.1. Characterization of electrodes

Materials were characterized using powder X-ray diffraction (PXRD), scanning electron microscopy (SEM, EDX), transmission electron microscopy (TEM), Raman spectroscopy (Renishaw), X-ray photoelectron spectroscopy (XPS), Auger electron spectroscopy (AES) and temperature programmed reduction (TPR). TPR studies were carried out using a customized TPR setup. Further details of the experimental setup are provided in the [supporting information](#) (Supplementary Note 2).

The Cu-impregnated samples were annealed at 800 °C and characterized using PXRD and electron microscopy (Fig. 2). Fig. 2(a) shows the membrane electrode assembly and cross-section SEM images showing the anodic and cathodic-electrolyte interfaces of NiO-YSZ/YSZ and LSM-YSZ/YSZ. The cathode and anode were sufficiently porous and adhered well to the electrolyte, as can be seen from Fig. S2. Comparing the Ni-YSZ and Ni{Cu}<sub>x</sub>-YSZ samples under SEM clearly shows that porosity in the Ni-Cu sample is reduced, as can be seen in Fig. S3. This is to be expected since Cu is infiltrated into the pores present in the Ni-YSZ framework. The overall effective TPB would be a function of both the nature of particle contacts, electronic conductivity and/or topological features such as porosity and tortuosity of the framework.

SEM-EDX mapping (Fig. 2(b)) indicates heterogeneity in Cu (Cu K $\alpha_1$ ) distribution on the Ni-YSZ surface upon impregnation of Cu. The change in the distribution of the elements in Ni{Cu}<sub>x</sub>O<sub>x</sub>-YSZ after CO<sub>2</sub> electrolysis can be seen in Figs. S4 and S5. SEM measurements were carried out at different depths of the cathode (Fig. S6). The redistribution of Ni and Cu in the Ni{Cu}<sub>x</sub>O<sub>x</sub>-YSZ samples after the CO<sub>2</sub> electrolysis can be seen from the depth profile of the elements in the cathode layer (Fig. S7).

TEM-EDX-based mapping (Fig. 2(c)) indicates that NiO particles are linked via YSZ linkages (co-localization of Zr and Y distribution is seen). Cu impregnation and annealing treatment results in complete coverage of NiO-YSZ surface by CuO. Fig. 2(d) shows the PXRD patterns of NiO-YSZ and Ni{Cu}<sub>x</sub>O<sub>x</sub>-YSZ. The NiO-YSZ sample compares well with NiO and YSZ reference spectra, indicating that the pure NiO phase is present alongside YSZ. The Ni{Cu}<sub>x</sub>O<sub>x</sub>-YSZ sample shows that this material is a combination of NiO, CuO and YSZ phases. Comparison of the peak shifts for these materials shows that the NiO(111) diffraction peak is shifted upon adding Cu indicating the mixing of Cu into the NiO lattice (Fig. 2(d), bottom panel). The PXRD patterns have been shown in detail in Figs. S8-S13. XPS measurements were carried out on NiO-YSZ and Ni{Cu}<sub>x</sub>O<sub>x</sub>-YSZ pre- and post-CO<sub>2</sub> electrolysis, and the corresponding data has been shown in detail in Figs. S14-S16.

### 2.1.1. Electrochemical characterization

A customized 2-chamber setup was used for electrochemical testing coupled with an online mass spectrometer as shown in Fig. S17(a).

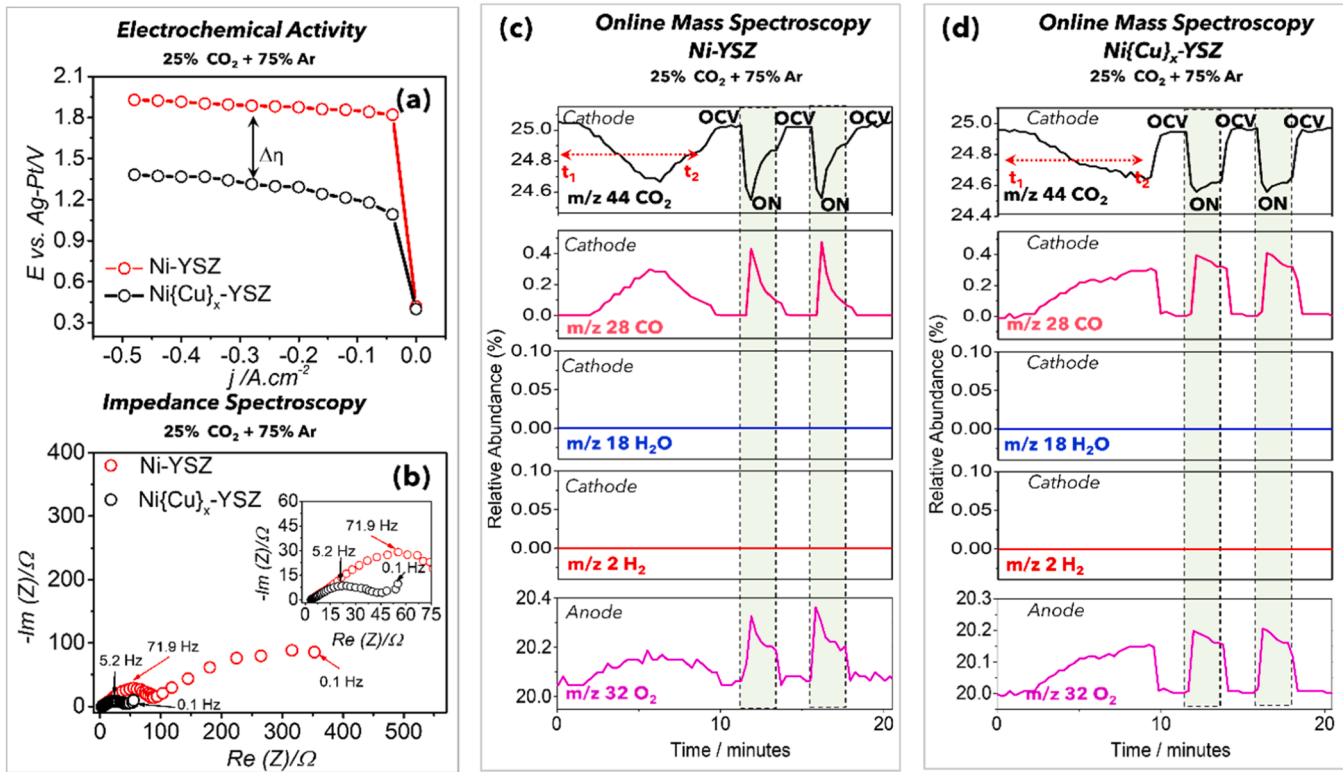
The cell was heated from 22 °C to 800 °C in artificial air (20% O<sub>2</sub> in Ar). Then cathode was subsequently reduced by using 5% H<sub>2</sub> in Ar. Concurrently, an artificial air atmosphere (20% O<sub>2</sub> in Ar) was maintained at the anode. The process was terminated when a stable open-circuit voltage (OCV) between the two electrodes was arrived at (1.1 V after ~15 min, Fig. S17(b)). The decay in the detected H<sub>2</sub>O signal confirmed the completion of the process (Fig. S17(c)).

Fig. 3(a) shows the current-voltage performance of CO<sub>2</sub> electrolysis at 800 °C for both Ni-YSZ and Ni{Cu}<sub>x</sub>-YSZ electrodes. The measurements were carried out in a 3-electrode geometry. The cathode voltage is reported vs. Ag/Pt electrode. A reduction current was progressively applied (current density J varied between 0 A/cm<sup>2</sup> and -0.48 A/cm<sup>2</sup>) in steps of 0.04 A/cm<sup>2</sup>. The current was held for 60 s at each step (Fig. S18(a-c) shows currents maintained for 240 s at each potential step; no differences in behavior were observed). Mass signals were monitored simultaneously for reactions at both the cathode and anode. Electrochemical Impedance Spectroscopy (EIS) measurements were carried out at various applied currents (including at OCV). The uncompensated resistance (R<sub>s</sub>) was extracted from the high-frequency intercept. All potentials have been corrected with the obtained R<sub>s</sub> value (E<sub>cathode</sub> = E<sub>applied</sub> - iR<sub>s</sub>) in Fig. 3(b). The progressive application of cathodic current on Ni-YSZ resulted in increased production of CO and consumption of CO<sub>2</sub> (Fig. 3(c)). This continued up to 0.24 A/cm<sup>2</sup> (@ 1.9 V vs. Ag/Pt). At currents higher than this value, the production of CO decreased, and the CO<sub>2</sub> consumption decreased as well, indicating deactivation. Subsequently, the cathode was switched between 0.48 A/cm<sup>2</sup> and open circuit (each condition was maintained for 3 min, while mass signals were continuously monitored). Application of 0.48 A/cm<sup>2</sup> resulted in an instant increase in CO production followed by immediate deactivation.

Cu infiltration into the Ni-YSZ electrode (Fig. 3(a)) resulted in a significant decrease in potential ( $\Delta\eta = 0.58$  V) required to achieve 0.24 A/cm<sup>2</sup> during pure CO<sub>2</sub> electrolysis. A substantial reduction in the polarization resistance was observed in the impedance spectra indicating superior electrocatalytic performance (Fig. 3(b)). The cathodic and anodic online mass signals from reactions from Ni-YSZ and Ni{Cu}<sub>x</sub>-YSZ electrodes during CO<sub>2</sub> electrolysis are shown in Fig. 3(c, d). In the case of Ni{Cu}<sub>x</sub>-YSZ cathode, there is a progressive increase in the amount of CO formation with an increase in applied current density. Unlike Ni-YSZ, the CO signal does not decay after 0.24 A/cm<sup>2</sup> but rather continues to increase all the way up to 0.48 A/cm<sup>2</sup>. Once at 0.48 A/cm<sup>2</sup>, the CO mass signal is reasonably maintained at a constant current. Contrastingly, in the case of the Ni-YSZ cathode (as discussed earlier), the onset of CO production (jump in CO production mass signal) upon stepping up to 0.48 A/cm<sup>2</sup> is immediately followed by a catastrophic decay in the CO formation signal.

### 2.1.2. Verification of electrode oxidation and Boudouard reaction

Previously, it has been proposed that Ni catalyst deactivation during



**Fig. 3.** Performance of Ni-YSZ and  $Ni\{Cu\}_x$ -YSZ cathodes. (a) Applied current vs. potential curves for electrochemical reduction of  $CO_2$ , (b) EIS plots under open-circuit conditions, Cathodic and anodic MS signal (c) Ni-YSZ (d)  $Ni\{Cu\}_x$ -YSZ, in the presence of 25%  $CO_2$  at 800 °C.

pure  $CO_2$  electrolytic reduction results from reactions such as Ni oxidation and Boudouard reaction (Fig. 4(a)). [9,13] The experimental scheme shown in Fig. 4(b) was used to probe the formation of  $C_x$  and metal oxide(s) species on the electrode surface from reactions (1) and (2) respectively. Mass signals were monitored during the entire scheme of experiments. In the reaction regime A, electrolysis was carried out at  $0.48 A/cm^2$  for the time duration of  $t_1 - t_2$ . The current was switched off and the electrode was allowed to stay in the  $CO_2$  atmosphere (25%  $CO_2$  in Ar) during  $t_2 - t_3$ . Then  $CO_2$  was switched off and the electrode was exposed to 100% Ar during  $t_3 - t_4$  (regime B). Subsequently, the electrodes were exposed to either 1%  $O_2$  (in Ar) (C') or 5%  $H_2$  (in Ar) (C).

Fig. 4(c-f) shows the above experimental scheme applied to Ni-YSZ and  $Ni\{Cu\}_x$ -YSZ electrodes. On Ni-YSZ, the introduction of 5%  $H_2$  resulted in the formation of  $H_2O$  on both electrodes, indicating that electrodes get oxidized during reaction regime A. The  $H_2O$  mass signal obtained from identical experiments on two different electrodes indicated that the amount of oxide formed on  $Ni\{Cu\}_x$ -YSZ is less compared to the Ni-YSZ electrode. The  $H_2O$  signal from the Cu-doped counterpart is not only smaller, but the reduction process also gets completed in half the time (~20 mins) as opposed to on the Ni-YSZ electrode. Similarly, exposure to 1%  $O_2$  resulted in developing a mass signal for  $CO_2$  ( $m/z = 44$ ), indicating that reaction regime A does result in the formation of  $C_x$  species on the surface of the Ni-YSZ electrode via the Boudouard reaction. No carbon deposit formation could be inferred on  $Ni\{Cu\}_x$ -YSZ using mass spectroscopy.

## 2.2. Impedance spectroscopy

To understand the improvement in the performance of  $Ni\{Cu\}_x$ -YSZ cathode, impedance spectra of Ni-YSZ and  $Ni\{Cu\}_x$ -YSZ cathode were recorded at different applied current densities during  $CO_2$  electrolysis. With an increase in current density, cell resistance decreased slightly, while a drastic reduction in polarization resistance was observed (Fig. 5(a)). Distribution of Relaxation Times (DRT) analysis was carried out on

EIS data to separate out contributions to the electron transfer processes at different timescales Fig. 5(b) [51]. In both electrodes, the DRT plot showed three distinct peaks. The high and middle frequency peaks respond strongly (albeit differently) to the applied current. They could be attributed to separate charge transfer processes, such as  $O^{2-}$  transfer across electrode-electrolyte interface, and/or dissociation of carbonate intermediate during  $CO_2$  electroreduction. The low-frequency peak does not respond to potential as strongly but becomes the dominant contributor to overall resistance at higher current densities. This is clearly observed on  $Ni\{Cu\}_x$ -YSZ electrode (Fig. 5(d)). This peak is likely associated with diffusive processes such as surface/pore diffusion [52, 53]. At high current densities, the reaction on  $Ni\{Cu\}_x$ -YSZ became essentially diffusion-limited with a large contribution from low-frequency component (Fig. 5(c, d)). The diffusion limitation of the reaction on  $Ni\{Cu\}_x$ -YSZ can be attributed either to a faster charge transfer or reduced porosity (Fig. S3). Comparing the plots at low current densities ( $-0.04 A/cm^2$ ), where Ni-YSZ is active, (Fig. 5(e, f)), the overall impedance was found to be lower for  $Ni\{Cu\}_x$ -YSZ electrode. Specifically, the difference between the electrodes originated from significantly lower charge transfer impedance on  $Ni\{Cu\}_x$ -YSZ compared to Ni-YSZ, indicating faster kinetics.

The lower value of high frequency intercepts of  $Ni\{Cu\}_x$ -YSZ, compared to Ni-YSZ, indicates the improved ballistic conduction in Ni-Cu sample [54]. Also, the Cu-infiltrated electrodes do not degrade in  $CO_2$  streams. We believe that the infiltration of Cu decreases the porosity, increases the electrical percolation length, and improves charge transfer (kinetics).

### 2.2.1. Operando Raman spectroscopy

A two-chamber setup designed in-house was used for operando Raman studies (Fig. 6(a)). The porous Ag current collector layer was partially removed from the top of the catalyst layer so that the  $NiO$ -YSZ particles could be directly visible under the Raman microscope, as is shown in Fig. S19. Sufficient conductivity was observed in active

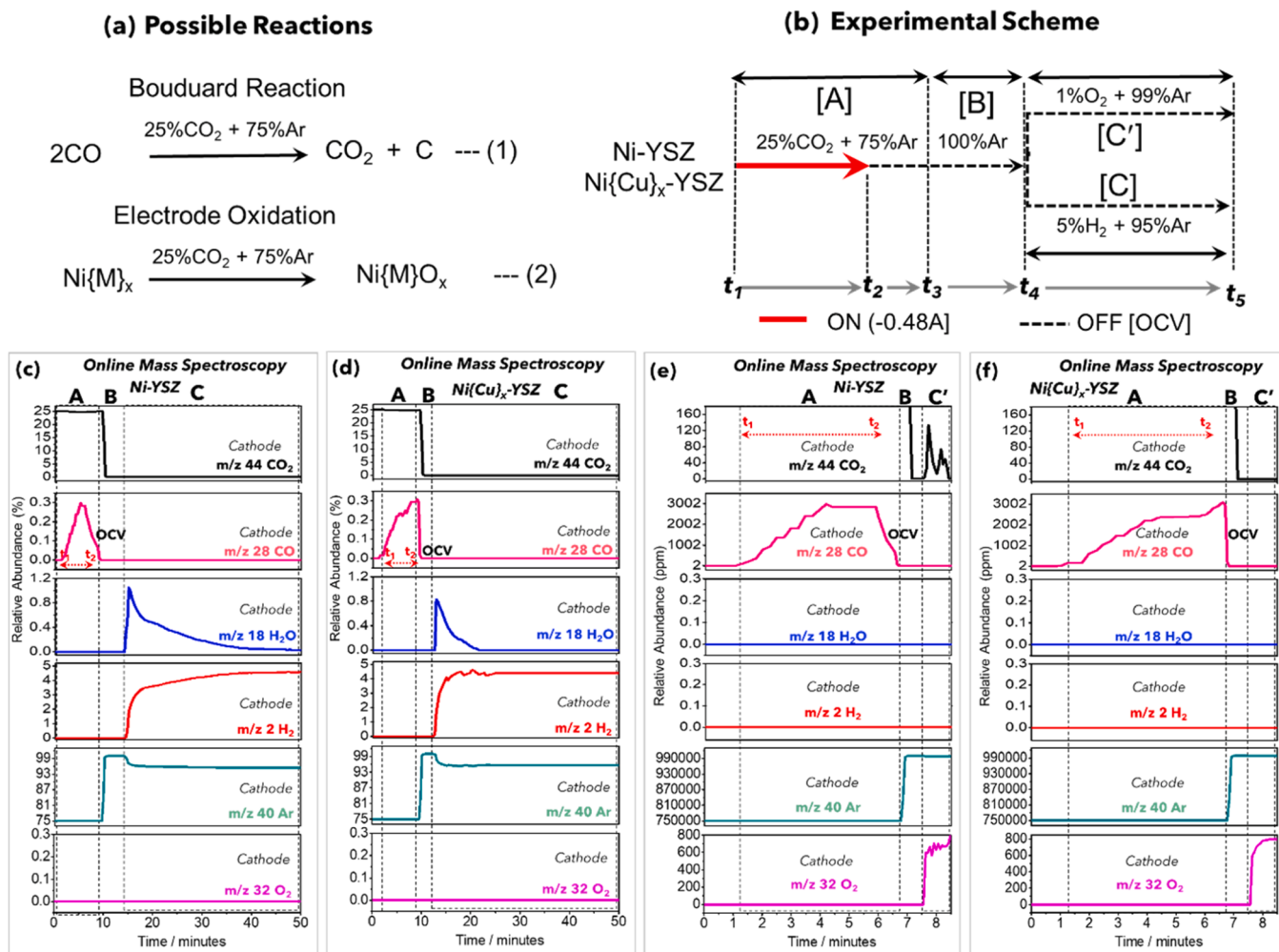


**Fig. 4.** (a) Possible side reactions during CO<sub>2</sub> electrolysis (b) Experimental Scheme to probe reactions mentioned in (a). After treating the catalyst at  $-0.48\text{ A/cm}^2$  under 25% CO<sub>2</sub>, the catalyst is treated at OCV under 100% Ar atmosphere. Subsequent treatment in 5% H<sub>2</sub> [C] and 1% O<sub>2</sub> [C'] was carried out to confirm the presence of oxides (NiO<sub>x</sub>/Ni<sub>x</sub>Cu<sub>y</sub>O<sub>z</sub>) and carbon on the electrode surface respectively. The mass signals from Ni-YSZ (c, e) and Ni<sub>x</sub>Cu<sub>y</sub>O<sub>z</sub>-YSZ (d, f) electrodes are shown.

samples (containing Ni or Ni<sub>x</sub>Cu<sub>y</sub>O<sub>z</sub>-YSZ) to maintain and monitor the triple-phase boundary regions that were electro-catalytically responsive. Studies by Kim. et al. have reported single chamber (cathode and anode on the same side) in situ Raman spectroscopic studies in the context of oxygen reduction reaction (ORR) [55,56]. We are reporting results from a two-chamber cell (cathode and anode in different atmospheres) that simulates the conditions likely to be found within a real electrolyzer. Optical images corresponding to NiO-YSZ and Ni<sub>x</sub>Cu<sub>y</sub>O<sub>z</sub>-YSZ cathodes are shown in Fig. 6(b, c). For NiO-YSZ, the surface was green in color, while Ni<sub>x</sub>Cu<sub>y</sub>O<sub>z</sub>-YSZ surface was golden along with the presence of dark spots, which have been shown in Fig. S20. The reported Raman spectra in Fig. 6(d) were recorded at 22 °C in artificial air (20% O<sub>2</sub> + 80% Ar). The spots for the Raman spectral collection have been marked with "x" and labeled with A', B' and B" as shown in Fig. 6(b, c). The spectrum of spot A' corresponds to the NiO-YSZ electrode with peaks at 146 cm<sup>-1</sup>, 225 cm<sup>-1</sup>, 319 cm<sup>-1</sup>, 460 cm<sup>-1</sup>, and 604 cm<sup>-1</sup> corresponding to vibration modes of YSZ. [57] The peak appearing at 562 cm<sup>-1</sup> corresponds to 1 P (1 phonon) oscillations in NiO. The peaks at ~725, 900, and 1082 cm<sup>-1</sup> are attributed to the 2 P oscillations in nickel oxide. Apart from this, the peak at ~1490 cm<sup>-1</sup> arises due to magnon (2 M) oscillations [58]. Raman spectra of B' spot shows peaks at 225, 534, 1074, 1372, and 1593 cm<sup>-1</sup>. We have performed Raman spectroscopy measurements on Ni<sub>x</sub>Cu<sub>y</sub>O<sub>z</sub> samples with varying Ni-Cu compositions (Fig. S21) to confirm that the peak at 534 cm<sup>-1</sup> appears due to the presence of Cu-doped Ni oxide (Cu alloyed into Ni oxide) [59–61]. Spectrum at B" on Ni<sub>x</sub>Cu<sub>y</sub>O<sub>z</sub>

O<sub>z</sub>-YSZ surface shows peaks at 294, 342, and 622 cm<sup>-1</sup> corresponding to A<sub>g</sub>, B<sub>g</sub>, and B<sub>g</sub> vibrational modes of CuO [62]. More details are available in Supplementary Note 3.

Fig. 6(e) shows the schematic diagrams of electrode surfaces of both pure Ni-YSZ and its Cu-infiltrated counterpart. Whereas the pure material is composed of NiO as expected, the Cu infiltrated material is heterogeneous at room temperatures with pure CuO patches (B") present on a Cu-doped nickel oxide surface (B') as confirmed using SEM-EDX mapping as shown in Fig. S4.

In situ Raman spectra collected during cell heating (22 °C temperature to 800 °C) are reported in Fig. 6(f-h). For NiO-YSZ, upon heating, the 2 M peak of NiO shifts to a lower wavenumber and eventually disappears at 200 °C, as per the well-known magnetic behavior of this material [63]. No significant change in material phase was observed other than the expected redshift shift of peaks with increasing temperature (due to volume expansion) [64]. The peak at 1082 cm<sup>-1</sup> redshifted by 31 cm<sup>-1</sup> upon heating to 800 °C. For Ni<sub>x</sub>Cu<sub>y</sub>O<sub>z</sub>, peaks around 1350–1595 cm<sup>-1</sup> corresponding to pore-forming carbon are completely removed by 800 °C as the sample is heated in air (Fig. 6(g)). The fact that these peaks are not observed while cooling the sample down to 22 °C after CO<sub>2</sub> electrolysis (Fig. S22) further confirms that they originated from the pore former. The CuO patches (Fig. 6(e)) remain upon heating to 800 °C.

Operando Raman spectroscopy of Ni-YSZ electrode was carried out post reductive treatment in 5% H<sub>2</sub> (at 800 °C), shown in Fig. S23(I). The

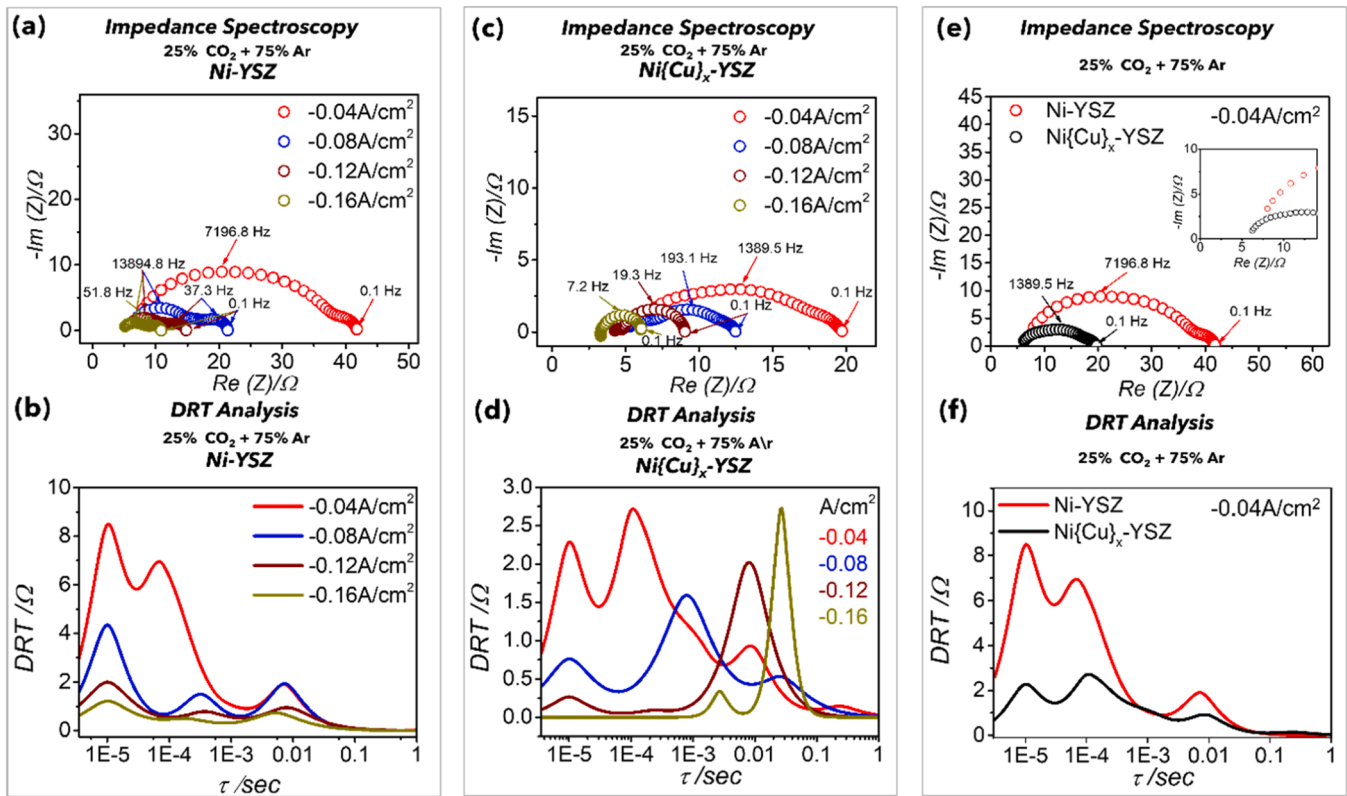


Fig. 5. : EIS under CO<sub>2</sub> electrolysis conditions for various applied current densities (a) Ni-YSZ (b) DRT plot for Ni-YSZ. (c) Ni<sub>x</sub>Cu<sub>1-x</sub>-YSZ (d) DRT plot for Ni<sub>x</sub>Cu<sub>1-x</sub>-YSZ (e) Comparison of Ni-YSZ and Ni<sub>x</sub>Cu<sub>1-x</sub>-YSZ electrodes at -0.04 A/cm<sup>2</sup>. (f) DRT plots of Ni-YSZ and Ni<sub>x</sub>Cu<sub>1-x</sub>-YSZ electrodes.

peaks including 599 cm<sup>-1</sup> can be assigned to YSZ, indicating that all Ni is present in a reduced metallic state (Fig. S23(I)). The reduced electrode was then exposed to 25% CO<sub>2</sub> (in Ar) at 800 °C and developed peaks at 343, 509, 684, and 1051 cm<sup>-1</sup> (Fig. S23(II)). These peaks can be attributed to the oxide of Ni, indicating that exposure to 25% CO<sub>2</sub> at 800 °C (at OCV) is sufficient to develop an oxide on Ni. The peaks at 343, 684, and 1051 cm<sup>-1</sup> appear in NiO (Fig. 6(f)). A strong peak at 509 cm<sup>-1</sup> was also observed. The PXRD pattern of this oxide (Fig. S8) matches with that of NiO. Also, Ni\_2p levels observed in XPS (Fig. S14) indicate similarity to NiO, implying that this is possibly a defective form of NiO, hereby referred to as NiO<sub>x</sub>. Song et al. and Chen and co-workers have also reported formation of NiO at open circuit potentials using ex-situ studies [13,46]. Subsequently, a reducing current was applied (-0.48 A/cm<sup>2</sup>) while the electrode was maintained in this atmosphere (25% CO<sub>2</sub>), simulating a condition where electrolysis happens under a strong reducing condition. Raman spectrum of this electrode (Fig. S23 (III)) only showed peaks corresponding to YSZ, while the NiO signal completely vanished indicating that NiO converts back to Ni under strongly reducing conditions (deactivated electrode). Song et al. have reported ex-situ studies where they have seen metallic Ni after operating the electrode in CO<sub>2</sub> atmosphere [13]. Chen et al. reported seeing a mixture of Ni and NiO using an XPS setup with a transfer chamber [46].

Operando Raman spectra were recorded at progressive cathodic current densities during CO<sub>2</sub> electrolysis (Fig. 7(a)). The electrode showed a strong NiO<sub>x</sub> signal at the open circuit. After progressively applying increasing cathodic currents, the NiO<sub>x</sub> signal intensity decreased and eventually vanished after 0.30 A/cm<sup>2</sup>. The detection of CO in the mass spectrometer exactly followed the same trend with respect to the applied currents. A direct correlation of the detected CO mass signal to the intensity of NiO<sub>x</sub> peaks on the electrode surface was observed. The CO production peaked at 0.24 A/cm<sup>2</sup> and then degraded. The NiO<sub>x</sub> signal on the electrode surface was observed from OCV up to 0.20 A/cm<sup>2</sup> and then begins to degrade coinciding with the decay of the

CO mass signal. A more detailed discussion has been carried out later in this section.

Upon switching the electrode between 0.48 A/cm<sup>2</sup> (strongly reducing condition) and OCV, the catalytic behaviour of CO<sub>2</sub> reduction along with deactivation of the electrode can be recreated. The Raman spectra on the Ni electrode shows that under conditions of electrolysis, NiO<sub>x</sub> gets regenerated when OCV is created and is completely removed once a strongly reducing current of 0.48 A/cm<sup>2</sup> is applied. Application of 0.48 A/cm<sup>2</sup> resulted in a spike in the CO signal immediately followed by a decay in the signal indicating that the electrode gets deactivated (Fig. 3(c)). Alternating the applied current between strongly reducing (0.48 A/cm<sup>2</sup>) and OCV showed that oxide creation was reversible (Fig. S24). The Raman spectra confirms it.

Fig. S25 shows Raman spectra of both the cathodes at OCV, collected in artificial air (20% O<sub>2</sub> + 80% Ar), followed by a reduction in (5% H<sub>2</sub> + 95% Ar), and subsequently in the presence of 25% CO<sub>2</sub> + 75% Ar. For the Ni-YSZ electrode (Fig. S25(a)), the NiO was observed in both artificial air and CO<sub>2</sub> (peaks in air and CO<sub>2</sub> are similar to the earlier noted difference in 509 cm<sup>-1</sup> peak), whereas in the presence of 5% H<sub>2</sub>, the oxide was completely reduced, and only peaks attributed to YSZ could be observed. In artificial air, the Raman spectrum at B' showed peaks at 520 and 1057 cm<sup>-1</sup> corresponding to the formation of Cu doped-Ni oxide (Fig. S25(b)) while B'' spot showed peaks at 273 and 316 cm<sup>-1</sup> corresponding to CuO as shown in Fig. S25(c). A reduction in 5% H<sub>2</sub> resulted in the complete removal of oxide peaks at both B' and B''. Exposure to CO<sub>2</sub> again resulted in the appearance of the same oxide peaks indicating oxidation in CO<sub>2</sub> in both Ni-YSZ and Ni<sub>x</sub>Cu<sub>1-x</sub>-YSZ electrodes.

During CO<sub>2</sub> electrolysis at 0.48 A/cm<sup>2</sup>, the Ni in Ni-YSZ, present as NiO<sub>x</sub> at OCV, is completely reduced back to metallic Ni (Fig. S23). For Ni<sub>x</sub>Cu<sub>1-x</sub>-YSZ, the application of 0.48 A/cm<sup>2</sup> results in changes at two different sites identified in Fig. 6(c). At B', the site which is composed of Cu-doped Ni oxide, the intensity of oxide peaks decreases but does not disappear ((Fig. S26(a))). At B'', the site which was rich in CuO, the peak

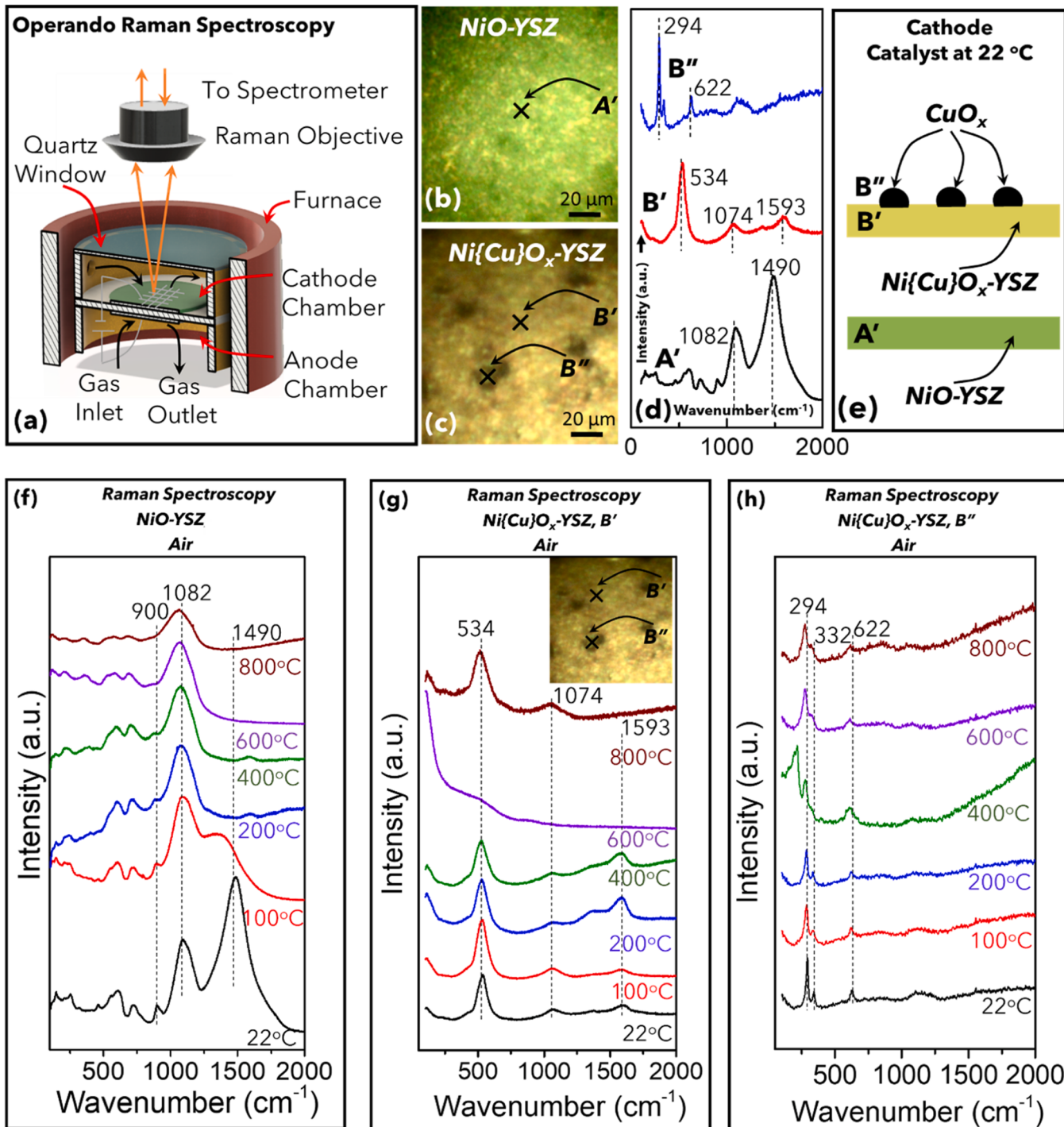


**Fig. 6.** : (a) Schematic diagram of operando Raman cell used in these studies. Optical images of (b)  $\text{NiO-YSZ}$  (c)  $\text{Ni}\{\text{Cu}\}\text{O}_x\text{-YSZ}$  (d) Raman spectra at the corresponding spots, (e) Schematic diagram of cathode architecture. Raman spectra of (f)  $\text{NiO-YSZ}$ , (g)  $\text{Ni}\{\text{Cu}\}\text{O}_x\text{-YSZ}$ , at  $B'$  site, and (h)  $\text{Ni}\{\text{Cu}\}\text{O}_x\text{-YSZ}$ , at  $B''$  site recorded at different temperatures during heating from 22 °C to 800 °C in artificial air (20%  $\text{O}_2$  + 80% Ar).

at 273  $\text{cm}^{-1}$  (corresponding to  $\text{CuO}$  peak) vanished completely, and the peak at 520  $\text{cm}^{-1}$  (corresponding to  $\text{Cu}$  doped  $\text{Ni}$  oxide) reduced in intensity (Fig. S26(b)). It was observed that sites like  $B''$  although initially rich in  $\text{CuO}$ , change in composition to  $B'$  type sites upon electrode cycling (reoxidation and reduction) (Fig. S27). Such sites ( $B''$ ) can be understood as those where  $\text{Cu}$  atoms have not completely mixed with  $\text{Ni}$  to form a mixed oxide during impregnation and consequent heat treatment. But eventually, as the electrode is repeatedly exposed to high temperatures (800 °C) and repeated oxidation and reduction processes, such  $\text{Cu}$ -rich sites eventually disappear due to diffusion of  $\text{Cu}$  into the

electrode, creating a mixed  $\text{Ni-Cu}$  material which when reoxidized (in  $\text{CO}_2$ ) results in the formation of  $\text{Cu-Ni}$  mixed oxide. Atomic percentages of  $\text{Cu}$  and  $\text{Ni}$  across the cross-section of  $\text{Ni}\{\text{Cu}\}\text{O}_x\text{-YSZ}$  cathode also confirm that  $\text{Cu}$  redistributes into the electrode uniformly (Fig. S7). Here on, we would primarily focus the discussion on  $B'$  ( $\text{Cu-doped Ni}$ ).

Operando Raman spectra of both the cathodes were collected at progressively increasing applied cathodic currents during  $\text{CO}_2$  electrolysis (Fig. 7 (a-c)). The intensities of representative peaks (for both electrodes) and the abundance of  $\text{CO}$  in the product stream have been plotted against the applied current density (Fig. 7(d)). The peaks

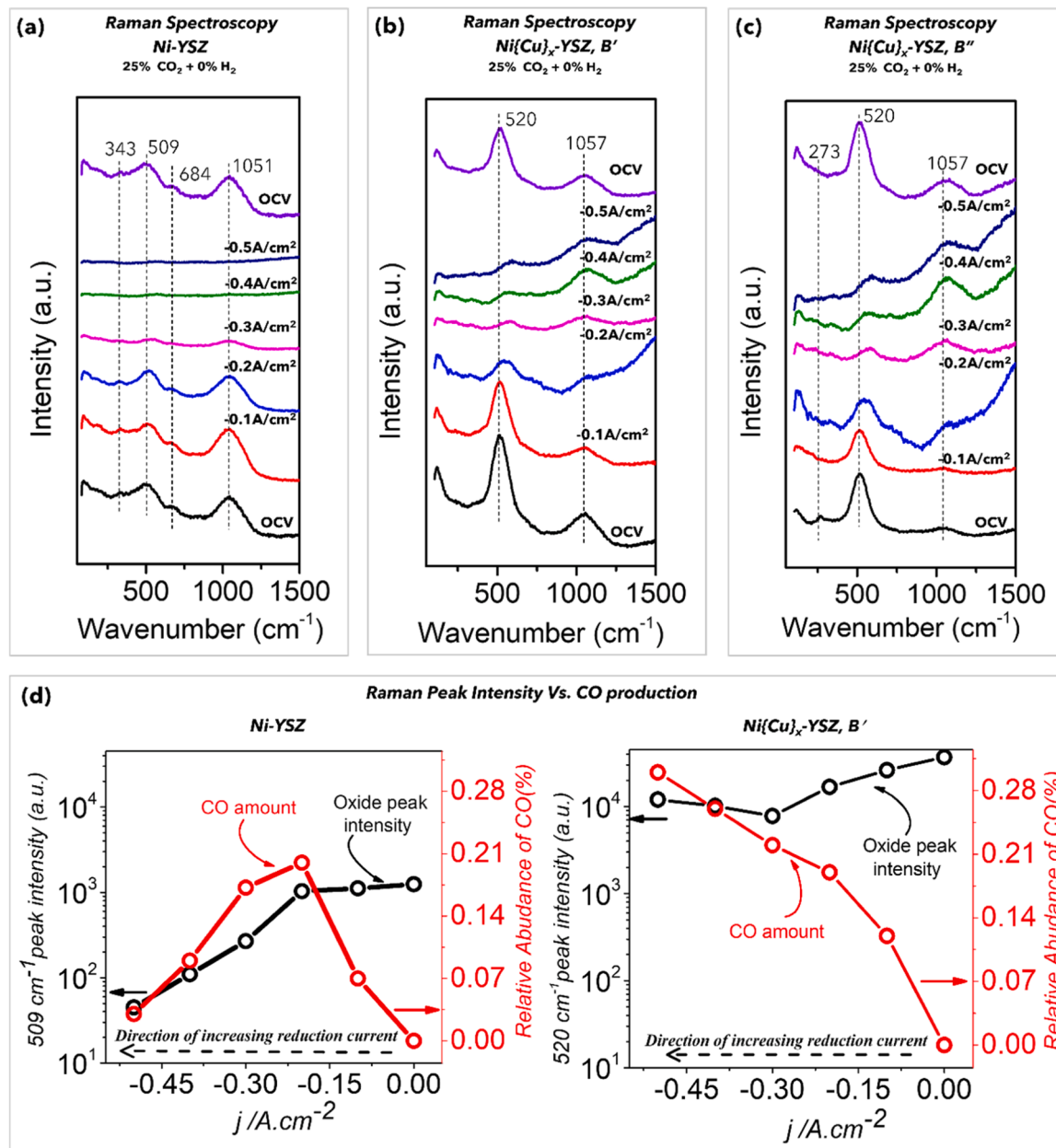


**Fig. 7.** Operando Raman Spectra during CO<sub>2</sub> electrolysis at various current densities. (a) Ni-YSZ electrode (b) Ni{Cu}<sub>x</sub>-YSZ, B' site (c) Ni{Cu}<sub>x</sub>-YSZ, B'' site, d) Raman peak intensity plotted against the abundance of CO in the product stream of various electrodes. Raman spectra at Ni-YSZ and Ni{Cu}<sub>x</sub>-YSZ, B' site are shown.

observed on the Ni-YSZ electrode (corresponding to NiO<sub>x</sub>) (Fig. 7(a, d)) decrease in intensity as the currents increase. The peaks are of negligible intensity by 0.30 A/cm<sup>2</sup> and completely disappear by 0.40 A/cm<sup>2</sup>. For the Ni{Cu}<sub>x</sub>-YSZ electrode (Fig. 7(b, d)), the peaks corresponding to Cu-doped Ni oxide slightly decrease in intensity with a progressive application of reduction current (in CO<sub>2</sub>) indicating that the electrode is partly reduced, but these peaks follow a different trend from pure Ni-YSZ. The oxide peaks from the Ni{Cu}<sub>x</sub> system stabilise in intensity around 0.30 A/cm<sup>2</sup>. Unlike Ni-YSZ electrode, these oxide peaks never disappear, and the CO production keeps increasing with increasing applied current, which is consistent with electrochemical activation behavior. At site B'', the peak at 273 cm<sup>-1</sup> (assigned to CuO) vanishes on applying 0.10 A/cm<sup>2</sup>, but the remaining set of peaks corresponding to Cu-doped Ni oxide show a behavior similar to that at B' (Fig. 7(c)). The behavior seen in Fig. 7(d) confirms that CO production on both electrodes correlates with oxide being present on the electrode surface. In the case of Ni-YSZ, such an oxide can be reduced to metallic Ni under

strongly reducing currents, resulting in deactivation of the electrode. In Ni{Cu}<sub>x</sub>-YSZ, such an oxide layer is more resistant to reduction and the electrode remains active for CO production, showing an expected electrochemically activated behavior.

This direct correlation of the CO signal to the intensity of NiO<sub>x</sub> on the Ni-YSZ electrode and the subsequent disappearance of CO mass signal along with the disappearance of NiO<sub>x</sub> from the electrode surface indicates that NiO<sub>x</sub> is the active catalyst material rather than metallic Ni, as previously believed. It is important to note that on Ni-YSZ at all points of time when the cathodic current is applied, and CO production occurs, the observed electrode is actually a combination of NiO<sub>x</sub> and metallic Ni. Such an electrode, if somehow frozen and successfully removed from the reaction chamber and measured ex-situ would indicate a presence of both NiO<sub>x</sub> and metallic Ni on the electrode surface. This result was also arrived at by Chen et al. using ex-situ XPS in combination with inert transfer methods [46]. Within such an experiment, it would still be impossible to attribute the activity to solely NiO<sub>x</sub>. This is likely to be the

reason that earlier ideas of metallic Ni being the active catalyst for pure CO<sub>2</sub> electrolysis and NiO<sub>x</sub> formation being the cause of deactivation have survived. It is only because our experiments are operando, that we are able to make a direct correlation between the existence of NiO<sub>x</sub> on the electrode and the detection of CO. This allows us to arrive at a different conclusion. The comparative study on Ni{Cu}<sub>x</sub>-YSZ electrode provides a perfect contrast to the deactivation behavior observed on Ni-YSZ. The presence of oxide and CO production on Ni{Cu}<sub>x</sub>-YSZ electrode at comparable potentials, where Ni-YSZ electrode undergoes deactivation due to the complete reduction of NiO<sub>x</sub>, directly implicates the oxide as the active catalytic material.

An alternating application of 0.48 A/cm<sup>2</sup> and OCV on both Ni-YSZ and Ni{Cu}<sub>x</sub>-YSZ electrodes is shown in Figs. S24 and S28. Whereas a complete removal of metal oxide is seen in Ni-YSZ upon application of 0.48 A/cm<sup>2</sup>, the oxide remains on Ni{Cu}<sub>x</sub>-YSZ electrode.

The H<sub>2</sub>O mass signal in Fig. 4(c, d), in combination with operando Raman spectroscopy indicates that the oxide layer formed on Ni{Cu}<sub>x</sub>-YSZ is thinner but more stable to electrochemical reduction under a CO<sub>2</sub> electrolysis environment. Although measurements using online MS on Ni-YSZ showed carbon deposition, no carbon deposition could be detected using Raman spectroscopy. Other ex-situ studies by Song et al. and Chen et al. also did not report seeing any carbon deposition post CO<sub>2</sub> electrolysis on Ni-YSZ [13,46]. MS remains a highly sensitive technique compared to Raman; it is likely that carbon deposition is not a major problem in this reaction, and carbon is only detectable when highly sensitive probes are used. No carbon deposit formation could be inferred through either mass spectroscopy or Raman spectroscopy on the Ni{Cu}<sub>x</sub>-YSZ cathode, indicating an absence of Boudouard reaction on this electrode.

Fig. S29(a, b) shows the current-voltage performance of Ni-YSZ and Ni{Cu}<sub>x</sub>-YSZ cathodes in two cycles of CO<sub>2</sub> electrolysis. Each cycle takes the electrodes from OCV up to 0.48 A/cm<sup>2</sup> at 0.04 A in each step and then creates an open circuit. A single cycle results in a substantial increase of overpotential at Ni-YSZ, indicating a significant loss of active sites during the previous cycle. A third such cycle could not be carried out on Ni-YSZ as the electrode completely degraded. It is likely that repeated oxidation (NiO<sub>x</sub> formation) and complete electrochemical reduction back to Ni may lead to the degradation of ionic connections, resulting in electrode breakdown. More information on the degradation of Ni-YSZ is available in Fig. S30. On the other hand, the Ni{Cu}<sub>x</sub>-YSZ electrode does not degrade with the same sequence of current cycling. The current potential curve during the second cycle exactly retraced the first, indicating no degradation. Furthermore, Ni{Cu}<sub>x</sub>-YSZ was tested for a duration of 50 h to check for long-term stability in pure CO<sub>2</sub> reduction. No deactivation or coke formation was detected (Fig. S29(e-h)).

## 2.2.2. Reducibility of metal oxides

In the light of results obtained from operando studies, further studies on the stability of NiO, CuO, and Ni{Cu}O<sub>x</sub> were carried out both using theoretical calculations (Fig. 8(a)) and temperature programmed reduction (TPR) experiments (Fig. 8(b)). Theoretical calculations (Density Functional Theory) which estimate oxygen abstraction energies from these oxides were carried out ( $E_{abs} = (E_0 + E_{MO}) - E_{MO}$ ) where  $E_{abs}$  is the energy of O abstraction (electronic energy),  $E_{MO}$  is the energy of the metal oxide,  $E_{MO'}$  is the energy of the defective metal oxide (where one oxygen atom has been removed), and  $E_0$  is the energy of a free oxygen atom. A higher abstraction energy implies a greater degree of difficulty in oxygen atom removal or higher oxophilicity of the particular oxide. It was observed that doping with Cu atoms resulted in the enhancement of  $E_{abs}$  of oxygen atoms within Ni-O-Ni bonds (by nearly 1.9 eV) (Fig. 8(a)). The oxygen bound to Ni-O-Cu bonds became slightly easier to abstract with  $E_{abs}$  of 4.76 eV compared to Ni-O-Ni bonds in pure NiO (at 5.03 eV). Calculations indicate that doping NiO with Cu results in a bimodal distribution of oxygen abstraction energies; whereas some oxygen atoms become slightly easier to abstract, other oxygen

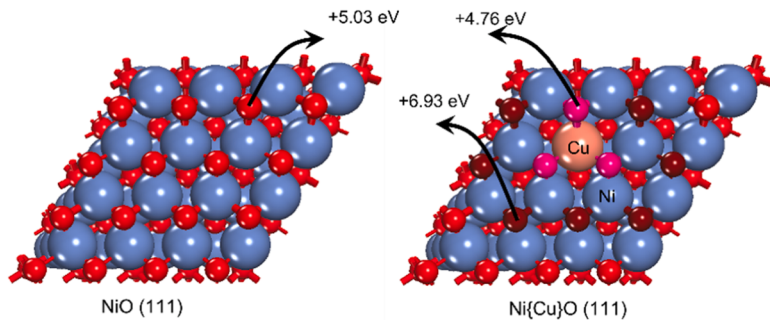
atoms, those within Ni-O-Ni become much more difficult to abstract.

The TPR experiments were performed on NiO, CuO, and Ni{Cu}O powders. These powders were synthesized using solution-based precursors (co-precipitation method), guaranteeing atomic-level mixing of metals within the metal oxide framework. More information on the synthesis and characterization of these powders is provided in the supporting information (Supplementary Note 2, III). TPR experiments using 3% H<sub>2</sub> (in Ar) were performed on various compositions of Ni<sub>1-x</sub>Cu<sub>x</sub>O<sub>x</sub> (Fig. 8 (b) and Figs. S31-S32). Measurements indicate that H<sub>2</sub>O removal peaks in pure NiO and pure CuO range between 274–563 °C and 220–547 °C respectively. Mixing NiO with Cu results in a bimodal distribution of oxygen removal signal (H<sub>2</sub>O signals). The sample with 50% Cu doping showed oxygen removal between 172–396 °C and between 396–653 °C. Such a distribution is also visible in other samples where Cu doping is between 10% and 40%. These experiments are consistent with theoretical calculations where doping with Cu within NiO seems to both reduce and increase O abstraction energies within the oxide. The high-temperature stability introduced by mixing Cu also gets reflected within the higher stability to reduction of Ni{Cu}O<sub>x</sub> electrodes. XPS and AES were used to probe the surface of the catalysts before and after CO<sub>2</sub> electrolysis (Figs. 8(c) and S14-S16). In the latter case, after CO<sub>2</sub> reduction the catalysts were brought to OCV and subsequently the electrode was cooled from 800 °C to room temperature in a CO<sub>2</sub> atmosphere (same as reaction atmosphere). Ni 2p spectra indicate that Ni retains essentially the same features before and after CO<sub>2</sub> electrolysis, an oxidation state of Ni<sup>2+</sup>. This is also similar to pure NiO/YSZ electrodes. The Cu 2p spectra in the pre-electrolysis sample have features similar to CuO, indicating Cu is in a +2 oxidation state. Post CO<sub>2</sub> reduction, the satellite features (945–940 eV) reduce in relative intensity, and the peak at 933.1 shifts to lower binding energies indicating the reduction of Cu. Distinguishing between Cu<sup>1+</sup> and Cu<sup>0</sup> remains challenging using Cu 2p spectra as binding energy differences are minute between the two. AES (Cu LMM) peaks better distinguish between Cu oxidation states. Peaks at 564 and 569 eV indicate that the sample has both Cu<sup>0</sup> and Cu<sup>2+</sup> in the sample. This implies that in Ni{Cu}O<sub>x</sub> electrode, Cu is in a reduced state post-electrolysis compared to the as-prepared Ni{Cu}O<sub>x</sub> before electrolysis.

## 2.2.3. Mechanism of CO<sub>2</sub> reduction

In oxide cathodes such as (La, Sr)(Co, Fe)O<sub>x</sub> and SmCeO<sub>x</sub>, it has been shown that CO<sub>2</sub> reduction proceeds via a carbonate type (3 coordinate carbon) intermediate. The presence of oxygen atoms on the surface of the catalysts plays a vital role in the formation of such a species [29,48, 49,65]. Scheme 1 shows the mechanism of CO<sub>2</sub> reduction on the surface of oxide electrodes. The surface oxygen, labelled  $\alpha$ , interacts with gas phase CO<sub>2</sub> to form a carbonate-type species. The presence of a vacancy nearby helps in cleaving the C-O bond with the oxygen atom inserting into the oxide surface and transferring to the ionic conductor. Opitz et al. have proposed a similar surface oxygen and surface vacancy mediated carbonate type species formation [48]. Ye et al. have also shown the formation of carbonate-type species on {La, Sr}TiO<sub>3-x</sub> using in situ IR spectroscopy in combination with TPD [18]. In oxides, the CO<sub>2</sub> reduction process essentially competes with the reduction of the metal. Feng et al. have shown that the surface of Sm<sub>x</sub>Ce<sub>1-x</sub>O<sub>2</sub> became enriched in Ce<sup>3+</sup> (~45%) upon application of cathodic overpotential under CO<sub>2</sub> reduction. The anodic polarization, on the other hand, results in Ce<sup>4+</sup> enriched surface [49]. Albrecht et al. have shown, using C k-edge NEXAFS on defective ceria (CeO<sub>1.7</sub>), CO<sub>2</sub> is preferentially adsorbed in the vicinity of Ce<sup>3+</sup> [66]. It is imperative that both surface oxygen species ( $\alpha$ ) and oxygen vacancy on the surface play an important role in the creation of a carbonate-type intermediate. Based on our studies, we propose that NiO<sub>x</sub> layer, created in situ under exposure to CO<sub>2</sub>, acts as the active catalyst for pure CO<sub>2</sub> reduction. Under reducing conditions, both CO<sub>2</sub> and NiO<sub>x</sub> are likely to be reduced, as shown in processes 1 and 2 respectively. Whereas the former is the desired reaction, the latter very likely assists in the process via the creation of vacancies that can interact

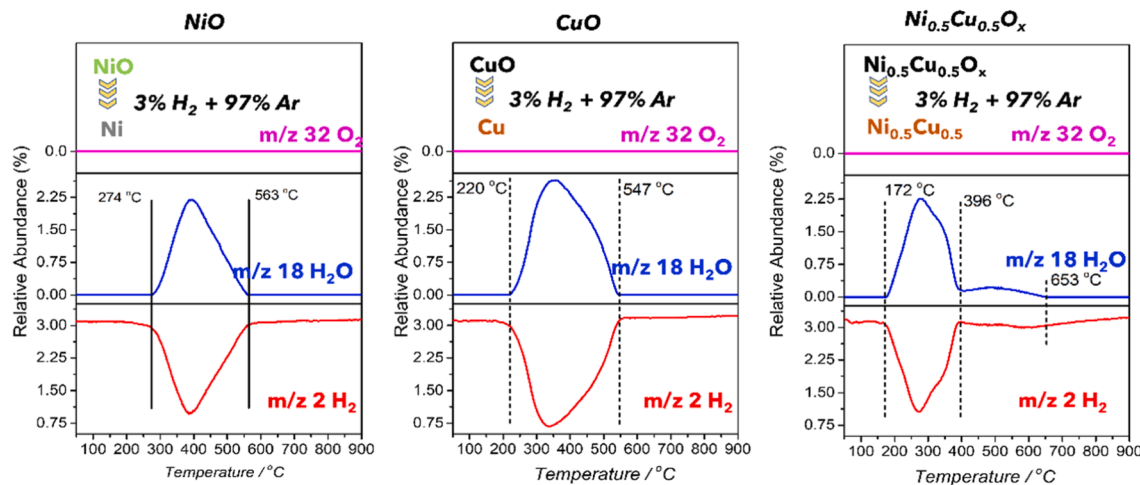
**(a) Calculated oxygen atom abstraction energy from NiO and Ni{Cu}O**



Bond	Type of linkage	Energy (in eV)
Ni-O in NiO(111)	Ni-O-Ni	+5.03
Ni-O in Ni{Cu}O(111)	Ni-O-Ni	+6.93
Ni-O-Cu	Ni-O-Cu	+4.76

**(b) Temperature Programmed Reactivity of NiO, CuO and Ni{Cu}O<sub>x</sub> in H<sub>2</sub>**

*Online Mass Spectroscopy*



**(c)**

**Surface Analysis (XPS and AES)**

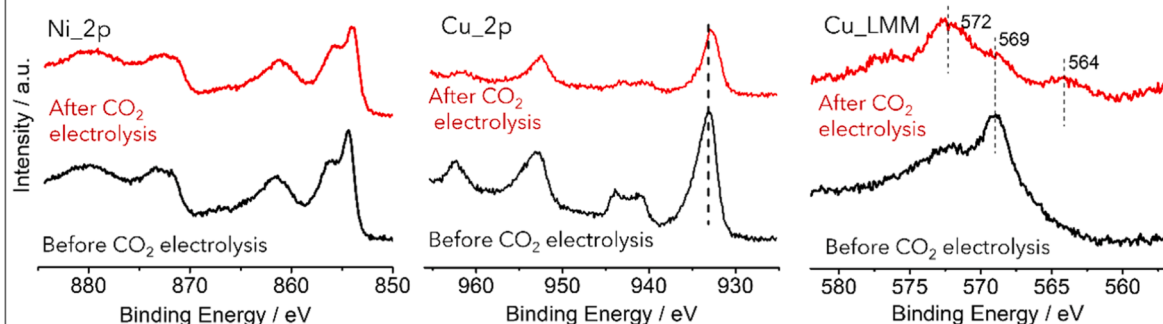
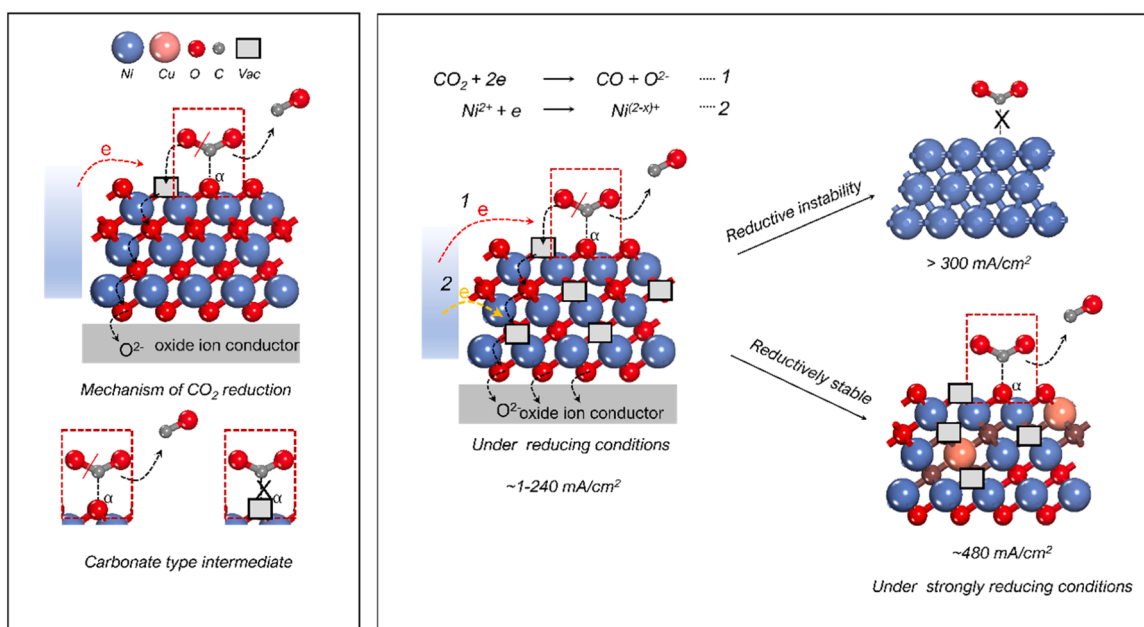


**Fig. 8. :** (a) Oxygen atom abstraction energies calculated from NiO and Ni{Cu}O structures. (b) Temperature programmed reduction in 3% H<sub>2</sub> (in Ar) for pure NiO, CuO, and Ni<sub>0.5</sub>Cu<sub>0.5</sub>O<sub>x</sub>. The mass signals for H<sub>2</sub>O (*m/z* 18), H<sub>2</sub> (*m/z* 2), and O<sub>2</sub> (*m/z* 32) were continuously monitored. (c) Ni 2p and Cu 2p, and Cu LMM signals for samples were collected before and after CO<sub>2</sub> electrolysis. The pre-electrolysis signals (black) are those from Ni{Cu}O oxide (post impregnation and annealing at 800 °C) before sample reduction, and post-electrolysis samples (red) were obtained by cooling the samples under 25% CO<sub>2</sub> (in Ar) at OCV.



**Scheme 1.** : Proposed mechanism for  $\text{CO}_2$  reduction on Ni electrodes is shown (left). The nature of electron transfer reactions (1, 2) is shown. Pure Ni shows reductive instability and reduces to Ni metal (at currents  $> 0.30 \text{ A/cm}^2$ ), which is inactive for  $\text{CO}_2$  reduction. The mixed Ni-Cu oxide has more strongly bound oxygen species on Ni which are reductively stable even at currents  $\sim 0.48 \text{ A/cm}^2$ .

with  $\text{CO}_2$ . A live catalyst is likely to have both species in balance.  $\text{NiO}_x$  catalyst does not degrade at currents of  $\sim 0.20 \text{ A/cm}^2$  and can successfully reduce  $\text{CO}_2$  to CO (Fig. S30). At higher current densities,  $> 0.24 \text{ A/cm}^2$ , the metal oxide reduction process seems to dominate, leading to a reduction in  $\alpha$  oxygen-type active sites and decrease in CO production. At currents approaching  $0.48 \text{ A/cm}^2$ , a complete reduction of oxide occurs, which does not allow  $\text{CO}_2$  to interact with the now pure Ni surface. The  $\text{Ni}\{\text{Cu}\}\text{O}_x$ , on the other hand, is much more difficult to reduce owing to difficulty in abstraction of oxygens within Ni-O-Ni linkages of the mixed oxide material. This allows the material to have stability even under strongly reducing conditions. The importance of surface oxygen for  $\text{CO}_2$  reduction is also highlighted by studies from Zhou et al. who have shown (using operando XANES/XAFS) that even in the aqueous medium, at ambient temperatures,  $\text{CO}_2$  reduction to products involves sites containing Ni-O bonds (with  $\text{Ni}^{6+}$ ) [67].

### 3. Conclusion

Using operando Raman and online mass spectrometry experiments, we have shown that pure  $\text{CO}_2$  electroreduction to CO on Ni-YSZ electrode proceeds on  $\text{NiO}_x$  (via an oxide-mediated mechanism) rather than on metallic Ni. When the electrode is placed under reaction conditions ( $800^\circ\text{C}$ ) at OCV,  $\text{CO}_2$  creates an oxide layer on the Ni surface, best labeled as  $\text{NiO}_x$ . It is this oxide layer that acts as the catalyst for  $\text{CO}_2$  reduction using surface oxygen species ( $\alpha$ ) and oxygen vacancies to create a carbonate type intermediate which can further undergo C-O bond cleavage. Under low applied currents, Ni-YSZ was found to be stable for CO production. Under stronger reduction bias ( $> 0.24 \text{ A/cm}^2$ ), the reduction of  $\text{NiO}_x$  becomes dominant over the reduction of  $\text{CO}_2$  and the catalyst begins to lose active sites resulting in decreased CO production. Under strongly reducing conditions (currents  $\sim 0.40 \text{ A/cm}^2$ ), the  $\text{NiO}_x$  completely reduces, and this coincides with stoppage in CO production. The Ni-O-Ni bond strength emerges as the primary descriptor of stability in pure  $\text{CO}_2$  streams.

Theoretical calculations using DFT and TPR experiments demonstrated that Nickel oxide stability significantly increases upon mixing Cu with Ni. The oxygen within the Ni-O-Ni linkages in  $\text{Ni}\{\text{Cu}\}\text{O}_x$  is significantly more stable to reduction compared to those within pure  $\text{NiO}_x$ .

Such an oxide survives under strongly reducing conditions and remains active for  $\text{CO}_2$  reduction. The  $\text{Ni}\{\text{Cu}\}\text{O}_x$ -YSZ electrode also demonstrated improved kinetics and greater stability against carbon deposition via the Boudouard reaction. Impedance analysis (DRT) suggests that the  $\text{Ni}\{\text{Cu}\}\text{O}_x$ -YSZ electrode shows significantly improved charge transfer characteristics compared to Ni-YSZ, which is responsible for the improved kinetic performance of the  $\text{Ni}\{\text{Cu}\}\text{O}_x$ -YSZ electrode.

### CRediT authorship contribution statement

**Vipin Kamboj:** Experimental work, Instrument design and fabrication, Data analysis, Writing – original draft, Writing – review & editing. **Soham Raychowdhury:** Theoretical calculations, Data analysis, Writing – original draft, Writing – review & editing. **Chinmoy Ranjan:** Conceptualisation, Methodology, Funding acquisition, Resources, Design of experiments, Instrument design, Data analysis, Writing – original draft, Writing – review & editing, Supervision.

### Declaration of Competing Interest

The authors declare the following financial interests/personal relationships which may be considered as potential competing interests. Chinmoy Ranjan reports financial support was provided by Department on Science and Technology India. Chinmoy Ranjan reports a relationship with Department of Science and Technology India that includes: funding grants.

### Data availability

Data will be made available on request.

### Acknowledgements

CR would like to thank the Department of Science and Technology (India) for the Mission Innovation Grant (IC5): Grant number: DST/TMD/(EWO)/IC5-2018/04 (G). CR would like to acknowledge DST-SERB CRG grant number: CRG/2019/0001586.

## Supporting Information

**Supporting information** contains details of experiments, characterization, theory, and spectroscopic and catalytic data.

## Appendix A. Supporting information

Supplementary data associated with this article can be found in the online version at [doi:10.1016/j.apcatb.2023.123631](https://doi.org/10.1016/j.apcatb.2023.123631).

## References

- [1] G.A. Florides, P. Christodoulides, Global warming and carbon dioxide through sciences, *Environ. Int.* 35 (2) (2009) 390–401, <https://doi.org/10.1016/j.envint.2008.07.007>.
- [2] D. Mattia, M.D. Jones, J.P. O’Byrne, O.G. Griffiths, R.E. Owen, E. Sackville, M. McManus, P. Plucinski, Towards carbon-neutral CO<sub>2</sub> conversion to hydrocarbons, *ChemSusChem* 8 (23) (2015) 4064–4072, <https://doi.org/10.1002/cssc.201500739>.
- [3] Z. Yuan, M.R. Eden, R. Gani, Toward the development and deployment of large-scale carbon dioxide capture and conversion processes, *Ind. Eng. Chem. Res.* 55 (12) (2016) 3383–3419, <https://doi.org/10.1021/acs.iecr.5b03277>.
- [4] S. Kar, A. Goeppert, V. Galvan, R. Chowdhury, J. Olah, G.K.S. Prakash, A Carbon-Neutral CO<sub>2</sub> Capture, Conversion, and Utilization Cycle with Low-Temperature Regeneration of Sodium Hydroxide, *J. Am. Chem. Soc.* 140 (49) (2018) 16873–16876, <https://doi.org/10.1021/jacs.8b09325>.
- [5] R. Küngas, Review—Electrochemical CO<sub>2</sub> Reduction for CO Production: Comparison of Low- and High-Temperature Electrolysis Technologies, *J. Electrochem. Soc.* 167 (4) (2020), 044508, <https://doi.org/10.1149/1945-7111/ab7099>.
- [6] S.D. Ebbesen, M. Mogensen, Electrolysis of carbon dioxide in solid oxide electrolysis cells, *J. Power Sources* 193 (1) (2009) 349–358, <https://doi.org/10.1016/j.jpowsour.2009.02.093>.
- [7] L. Chen, F. Chen, C. Xia, Direct Synthesis of Methane from CO<sub>2</sub>-H<sub>2</sub>O Co-Electrolysis in Tubular Solid Oxide Electrolysis Cells, *Energy Environ. Sci.* 7 (12) (2014) 4018–4022, <https://doi.org/10.1039/c4ee02786h>.
- [8] K. Xie, Y. Zhang, G. Meng, J.T.S. Irvine, Direct Synthesis of Methane from CO<sub>2</sub>/H<sub>2</sub>O in an Oxygen-Ion Conducting Solid Oxide Electrolyser, *Energy Environ. Sci.* 4 (6) (2011) 2218–2222, <https://doi.org/10.1039/clee01035b>.
- [9] F. Bidrawn, G. Kim, G. Corre, J.T.S. Irvine, J.M. Vohs, R.J. Gorte, Efficient Reduction of CO<sub>2</sub> in a Solid Oxide Electrolyzer, *Electrochim. Solid-State Lett.* 11 (9) (2008), <https://doi.org/10.1149/1.2943664>.
- [10] L. Sun, Q. Zheng, N. Li, C. Chen, Z. Zhan, Direct Electrolysis of CO<sub>2</sub> in Solid Oxide Cells Supported on Ceramic Fuel Electrodes with Straight Open Pores and Coated Catalysts, *Solid State Ion.-* 344 (2020), 115154, <https://doi.org/10.1016/j.ssi.2019.115154>.
- [11] P. Hjalmarsson, X. Sun, Y.-L. Liu, M. Chen, Durability of High Performance Ni-Yttria Stabilized Zirconia Supported Solid Oxide Electrolysis Cells at High Current Density, *J. Power Sources* 262 (2014) 316–322, <https://doi.org/10.1016/j.jpowsour.2014.03.133>.
- [12] S. Xu, S. Li, W. Yao, D. Dong, K. Xie, Direct Electrolysis of CO<sub>2</sub> Using an Oxygen-Ion Conducting Solid Oxide Electrolyzer Based on La0.75Sr0.25Cr 0.5Mn0.5O<sub>3</sub> - δ Electrode, *J. Power Sources* 230 (2013) 115–121, <https://doi.org/10.1016/j.jpowsour.2012.12.068>.
- [13] Y. Song, Z. Zhou, X. Zhang, Y. Zhou, H. Gong, H. Lv, Q. Liu, G. Wang, X. Bao, C. O. Pure, 2 Electrolysis over an Ni/YSZ Cathode in a Solid Oxide Electrolysis Cell, *J. Mater. Chem. A* 6 (28) (2018) 13661–13667, <https://doi.org/10.1039/C8TA02858C>.
- [14] X. Li, Y. Wang, W. Liu, J.A. Wilson, J. Wang, C. Wang, J. Yang, C. Xia, X.-D. Zhou, W. Guan, Reliability of CO<sub>2</sub> Electrolysis by Solid Oxide Electrolysis Cells with a Flat Tube Based on a Composite Double-Sided Air Electrode, *Compos. Part B Eng.* 166 (2019) 549–554, <https://doi.org/10.1016/j.compositesb.2019.02.012>.
- [15] M.C. Azucena Nepomuceno, Y. Kato, Development of Disk-Type Solid Oxide Electrolysis Cell for CO<sub>2</sub> Reduction in an Active Carbon Recycling Energy System, *Energy Procedia* 131 (2017) 101–107, <https://doi.org/10.1016/j.egypro.2017.09.480>.
- [16] J.-Y. Ahn, B.-K. Kim, J.-S. Park, Effects of metal catalysts on co-electrolysis of steam and carbon dioxide, *J. Electrochim. Soc.* 163 (10) (2016) F1288–F1293, <https://doi.org/10.1149/2.1321610jes>.
- [17] Q. Fu, C. Mabilat, M. Zahid, A. Brisse, L. Gautier, Syngas Production via High-Temperature Steam/CO<sub>2</sub> Co-Electrolysis: An Economic Assessment, *Energy Environ. Sci.* 3 (10) (2010) 1382, <https://doi.org/10.1039/c0ee00092b>.
- [18] L. Ye, M. Zhang, P. Huang, G. Guo, M. Hong, C. Li, J.T.S. Irvine, K. Xie, Enhancing CO<sub>2</sub> Electrolysis through Synergistic Control of Non-Stoichiometry and Doping to Tune Cathode Surface Structures, *Nat. Commun.* 8 (1) (2017) 10, <https://doi.org/10.1038/ncomms14785>.
- [19] S.D. Ebbesen, R. Knibbe, M. Mogensen, Co-electrolysis of steam and carbon dioxide in solid oxide cells, *J. Electrochim. Soc.* 159 (8) (2012) F482–F489, <https://doi.org/10.1149/2.076208jes>.
- [20] Y. Wang, T. Liu, S. Fang, F. Chen, Syngas Production on a Symmetrical Solid Oxide H<sub>2</sub>O/CO<sub>2</sub> Co-Electrolysis Cell with Sr<sub>2</sub>Fe<sub>1.5</sub>Mn<sub>0.5</sub>O<sub>6</sub>-Sm<sub>0.2</sub>Ce<sub>0.8</sub>O<sub>1.9</sub>
- [21] J. Xu, X. Zhou, J. Cheng, L. Pan, M. Wu, X. Dong, K. Sun, Electrochemical Performance of Highly Active Ceramic Symmetrical Electrode La<sub>0.3</sub>Sr<sub>0.7</sub>Ti<sub>0.3</sub>P<sub>0.7</sub>O<sub>3</sub>-δ-CeO<sub>2</sub> for Reversible Solid Oxide Cells, *Electrochim. Acta* 257 (2017) 64–72, <https://doi.org/10.1016/j.electacta.2017.10.061>.
- [22] X. Yue, J.T.S. Irvine, (La,Sr)(Cr,Mn)O<sub>3</sub>/GDC Cathode for High Temperature Steam Electrolysis and Steam-Carbon Dioxide Co-Electrolysis, *Solid State Ion.-* 225 (2012) 131–135, <https://doi.org/10.1016/j.ssi.2012.06.015>.
- [23] K. Lillmaa, M. Maide, R. Kanarbik, G. Nurk, E. Lust, Electrochemical Characteristics and Gas Composition Generated by La<sub>0.8</sub> Sr<sub>0.2</sub> Cr<sub>0.5</sub> Mn<sub>0.5</sub> O<sub>3</sub>-δ Cathode at Electrolysis and Co-Electrolysis Modes, *J. Electrochim. Soc.* 163 (11) (2016) F3190–F3196, <https://doi.org/10.1149/2.0261611jes>.
- [24] S.-E. Yoon, S.-H. Song, J. Choi, J.-Y. Ahn, B.-K. Kim, J.-S. Park, Coelectrolysis of Steam and CO<sub>2</sub> in a Solid Oxide Electrolysis Cell with Ceramic Composite Electrodes, *Int. J. Hydrol. Energy* 39 (11) (2014) 5497–5504, <https://doi.org/10.1016/j.ijhydene.2014.01.124>.
- [25] S.-E. Yoon, J.-Y. Ahn, B.-K. Kim, J.-S. Park, Improvements in co-electrolysis performance and long-term stability of solid oxide electrolysis cells based on ceramic composite cathodes, *Int. J. Hydrol. Energy* 40 (39) (2015) 13558–13565, <https://doi.org/10.1016/j.ijhydene.2015.08.012>.
- [26] P.K. Addo, B. Molero-Sánchez, M. Chen, S. Paulson, V. Birss, CO/CO<sub>2</sub> Study of High Performance La<sub>0.3</sub>Sr<sub>0.7</sub>Fe<sub>0.7</sub>Cr<sub>0.3</sub>O<sub>3</sub>-δ Reversible SOFC Electrodes, *Fuel Cells* 15 (5) (2015) 689–696, <https://doi.org/10.1002/fuce.201400196>.
- [27] Y. Li, P. Li, B. Hu, C. Xia, A Nanostructured Ceramic Fuel Electrode for Efficient CO<sub>2</sub>/H<sub>2</sub>O Electrolysis without Safe Gas, *J. Mater. Chem. A* 4 (23) (2016) 9236–9243, <https://doi.org/10.1039/C6TA02830F>.
- [28] W. Wang, L. Gan, J.P. Lemmon, F. Chen, J.T.S. Irvine, K. Xie, Enhanced carbon dioxide electrolysis at redox manipulated interfaces, *Nat. Commun.* 10 (1) (2019) 1–10, <https://doi.org/10.1038/s41467-019-10568-1>.
- [29] Y. Yu, B. Mao, A. Geller, R. Chang, K. Gaskell, Z. Liu, B.W. Eichhorn, CO<sub>2</sub> Activation and Carbonate Intermediates: An Operando AP-XPS Study of CO<sub>2</sub> Electrolysis Reactions on Solid Oxide Electrochemical Cells, *Phys. Chem. Chem. Phys.* 16 (23) (2014) 11633–11639, <https://doi.org/10.1039/C4CP01054J>.
- [30] M. Chen, Y.-L. Liu, J.J. Bentzen, W. Zhang, X. Sun, A. Hauch, Y. Tao, J.R. Bowen, P. V. Hendriksen, Microstructural Degradation of Ni/YSZ Electrodes in Solid Oxide Electrolysis Cells under High Current, *J. Electrochim. Soc.* 160 (8) (2013) F883–F891, <https://doi.org/10.1149/2.098308jes>.
- [31] Y. Tao, S.D. Ebbesen, M.B. Mogensen, Degradation of solid oxide cells during co-electrolysis of steam and carbon dioxide at high current densities, *J. Power Sources* 328 (2016) 452–462, <https://doi.org/10.1016/j.jpowsour.2016.08.055>.
- [32] R. Knibbe, M.L. Traulsen, A. Hauch, S.D. Ebbesen, M. Mogensen, Solid oxide electrolysis cells: degradation at high current densities, *J. Electrochim. Soc.* 157 (8) (2010) B1209, <https://doi.org/10.1149/1.3447752>.
- [33] A.R. Hanifi, M.A. Laguna-Bercero, N.K. Sandhu, T.H. Etzell, P. Sarkar, Tailoring the microstructure of a solid oxide fuel cell anode support by calcination and milling of YSZ, *Sci. Rep.* 6 (1) (2016), 27359, <https://doi.org/10.1038/srep27359>.
- [34] Z. Cheng, J.-H. Wang, Y. Choi, L. Yang, M.C. Lin, M. Liu, From Ni-YSZ to Sulfur-Tolerant Anode Materials for SOFCs: Electrochemical Behavior, In Situ Characterization, Modeling, and Future Perspectives, *Energy Environ. Sci.* 4 (11) (2011) 4380, <https://doi.org/10.1039/clee01758f>.
- [35] D. Dong, S. Xu, X. Shao, L. Hucker, J. Marin, T. Pham, K. Xie, Z. Ye, P. Yang, L. Yu, G. Parkinson, C.-Z. Li, Hierarchically Ordered Porous Ni-Based Cathode-Supported Solid Oxide Electrolysis Cells for Stable CO<sub>2</sub> Electrolysis without Safe Gas, *J. Mater. Chem. A* 5 (46) (2017) 24098–24102, <https://doi.org/10.1039/C7TA06839E>.
- [36] J. Yan, H. Chen, E. Dogdibegovic, J.W. Stevenson, M. Cheng, X.-D. Zhou, High-Efficiency Intermediate Temperature Solid Oxide Electrolyzer Cells for the Conversion of Carbon Dioxide to Fuels, *J. Power Sources* 252 (2014) 79–84, <https://doi.org/10.1016/j.jpowsour.2013.11.047>.
- [37] Y. Li, J. Zhou, D. Dong, Y. Wang, J.Z. Jiang, H. Xiang, K. Xie, Composite Fuel Electrode La<sub>0.25</sub>Sr<sub>0.75</sub>TiO<sub>3</sub>-δ-Ce<sub>0.8</sub>Sm<sub>0.2</sub>O<sub>2</sub>-δ for Electrolysis of CO<sub>2</sub> in an Oxygen-Ion Conducting Solid Oxide Electrolyser, *Phys. Chem. Chem. Phys.* 14 (44) (2012) 15547, <https://doi.org/10.1039/c2cp42232h>.
- [38] Y. Tao, S.D. Ebbesen, M.B. Mogensen, Carbon Deposition in Solid Oxide Cells during Co-Electrolysis of H<sub>2</sub>O and CO<sub>2</sub>, *J. Electrochim. Soc.* 161 (3) (2014) F337, <https://doi.org/10.1149/2.079403jes>.
- [39] P. Kim-Lohsoontorn, J. Bae, Electrochemical Performance of Solid Oxide Electrolysis Cell Electrodes under High-Temperature Coelectrolysis of Steam and Carbon Dioxide, *J. Power Sources* 196 (17) (2011) 7161–7168, <https://doi.org/10.1016/j.jpowsour.2010.09.018>.
- [40] W. Li, H. Wang, Y. Shi, N. Cai, Performance and Methane Production Characteristics of H<sub>2</sub>O-CO<sub>2</sub> Co-Electrolysis in Solid Oxide Electrolysis Cells, *Int. J. Hydrol. Energy* 38 (25) (2013) 11104–11109, <https://doi.org/10.1016/j.ijhydene.2013.01.008>.
- [41] C. Graves, S.D. Ebbesen, M. Mogensen, Co-Electrolysis of CO<sub>2</sub> and H<sub>2</sub>O in Solid Oxide Cells: Performance and Durability, *Solid State Ion.-* 192 (1) (2011) 398–403, <https://doi.org/10.1016/j.ssi.2010.06.014>.
- [42] V. Singh, H. Muroyama, T. Matsui, S. Hashigami, T. Inagaki, K. Eguchi, Feasibility of alternative electrode materials for high temperature CO<sub>2</sub> reduction on solid oxide electrolysis cell, *J. Power Sources* 293 (2015) 642–648, <https://doi.org/10.1016/j.jpowsour.2015.05.088>.
- [43] V. Singh, H. Muroyama, T. Matsui, K. Eguchi, Performance and Stability of Solid Oxide Electrolysis Cell for CO<sub>2</sub> Reduction under Various Operating Conditions, *Electrochemistry* 82 (10) (2014) 839–844, <https://doi.org/10.5796/electrochemistry.82.839>.

[44] S.D. Ebbesen, C. Graves, A. Hauch, S.H. Jensen, M. Mogensen, Poisoning of Solid Oxide Electrolysis Cells by Impurities, *J. Electrochem. Soc.* 157 (10) (2010) B1419, <https://doi.org/10.1149/1.3464804>.

[45] L. Yu, J. Wang, X. Hu, Z. Ye, C. Buckley, D. Dong, A Nanocatalyst Network for Electrochemical Reduction of CO<sub>2</sub> over Microchanneled Solid Oxide Electrolysis Cells, *Electrochim. Commun.* 86 (2018) 72–75, <https://doi.org/10.1016/j.elecom.2017.11.019>.

[46] D. Chen, J. Zhang, M. Barreau, S. Turczyniak-Surdacka, O. Joubert, A.L.G. La Salle, S. Zafeiratos, Ni-Doped CeO<sub>2</sub> Nanoparticles to Promote and Restore the Performance of Ni/YSZ Cathodes for CO<sub>2</sub> Electroreduction, *Appl. Surf. Sci.* 611 (2023), 155767, <https://doi.org/10.1016/j.apsusc.2022.155767>.

[47] L. Ye, X. Hu, X. Wang, F. Chen, D. Tang, D. Dong, K. Xie, Enhanced CO<sub>2</sub> Electrolysis with a SrTiO<sub>3</sub> Cathode through a Dual Doping Strategy, *J. Mater. Chem. A* 7 (6) (2019) 2764–2772, <https://doi.org/10.1039/c8ta10188d>.

[48] A.K. Opitz, A. Nenning, C. Rameshan, M. Kubicek, T. Götsch, R. Blume, M. Hävecker, A. Knop-Gericke, G. Rupprechter, B. Klötzer, J. Fleig, Surface Chemistry of Perovskite-Type Electrodes during High Temperature CO<sub>2</sub> Electrolysis Investigated by Operando Photoelectron Spectroscopy, *ACS Appl. Mater. Interfaces* 9 (41) (2017) 35847–35860, <https://doi.org/10.1021/acsami.7b10673>.

[49] Z.A. Feng, M.L. Machala, W.C. Chueh, Surface Electrochemistry of CO<sub>2</sub> Reduction and CO Oxidation on Sm-Doped CeO<sub>2-x</sub>: Coupling between Ce<sup>3+</sup> and Carbonate Adsorbates, *Phys. Chem. Chem. Phys.* 17 (18) (2015) 12273–12281, <https://doi.org/10.1039/CSCP00114E>.

[50] J. Rutman, I. Riess, Placement of Reference Electrode in Solid State Electrolyte Cells, *Solid State Ion.-* 179 (21–26) (2008) 913–918, <https://doi.org/10.1016/j.ssi.2008.01.071>.

[51] T.H. Wan, M. Saccoccia, C. Chen, F. Ciucci, Influence of the Discretization Methods on the Distribution of Relaxation Times Deconvolution: Implementing Radial Basis Functions with DRTtools, *Electrochim. Acta* 184 (2015) 483–499, <https://doi.org/10.1016/j.electacta.2015.09.097>.

[52] X. Zhang, Y. Song, F. Guan, Y. Zhou, H. Lv, G. Wang, X. Bao, Enhancing Electrocatalytic CO<sub>2</sub> Reduction in Solid Oxide Electrolysis Cell with Ce<sub>0.9</sub>Mn<sub>0.1</sub>O<sub>2-δ</sub> Nanoparticles-Modified LSCM-GDC Cathode, *J. Catal.* 359 (2018) 8–16, <https://doi.org/10.1016/j.jcat.2017.12.027>.

[53] H. Lv, Y. Zhou, X. Zhang, Y. Song, Q. Liu, G. Wang, X. Bao, Infiltration of Ce<sub>0.8</sub>Gd<sub>0.2</sub>O<sub>1.9</sub> Nanoparticles on Sr<sub>2</sub>Fe<sub>1.5</sub>Mo<sub>0.5</sub>O<sub>6</sub>- Cathode for CO<sub>2</sub> Electroreduction in Solid Oxide Electrolysis Cell, *J. Energy Chem.* 35 (2019) 71–78, <https://doi.org/10.1016/j.jechem.2018.11.002>.

[54] S.B. Adler, Factors governing oxygen reduction in solid oxide fuel cell cathodes, *Chem. Rev.* 104 (10) (2004) 4791–4844, <https://doi.org/10.1021/cr020724o>.

[55] J.H. Kim, S. Yoo, R. Murphy, Y. Chen, Y. Ding, K. Pei, B. Zhao, G. Kim, Y. Choi, M. Liu, Promotion of oxygen reduction reaction on a double perovskite electrode by a water-induced surface modification, *Energy Environ. Sci.* 14 (3) (2021) 1506–1516, <https://doi.org/10.1039/D0EE03283B>.

[56] X. Li, K. Blinn, D. Chen, M. Liu, In Situ and Surface-Enhanced Raman Spectroscopy Study of Electrode Materials in Solid Oxide Fuel Cells, *Electrochim. Energy Rev.* 1 (3) (2018) 433–459, <https://doi.org/10.1007/s41918-018-0017-9>.

[57] A. Naumenko, N. Berezovska, M. Biliy, O.V. Shevchenko, Vibrational Analysis and Raman Spectra of Tetragonal Zirconia, *Phys. Chem. Solid State* 9 (2008) 121–125.

[58] N. Mironova-Ulmane, A. Kuzmin, I. Sildos, L. Puust, J. Grabis, Magnon and Phonon Excitations in Nanosized NiO, *Latv. J. Phys. Tech. Sci.* 56 (2) (2019) 61–72, <https://doi.org/10.2478/lpts-2019-0014>.

[59] X. Yang, W. Liu, G. Pan, Y. Sun, Modulation of Oxygen in NiO:Cu Films toward a Physical Insight of NiO:Cu/c-Si Heterojunction Solar Cells, *J. Mater. Sci.* 53 (16) (2018) 11684–11693, <https://doi.org/10.1007/s10853-018-2430-1>.

[60] V.K. Yadav, H.P. Shinde, T. Das, Oxidation of Cyclohexane Using Copper-Nickel Catalyst, *Arab. J. Sci. Eng.* (2021), <https://doi.org/10.1007/s13369-021-05547-1>.

[61] R. Liaqat, M.A. Mansoor, J. Iqbal, A. Jilani, S. Shakir, A. Kalam, S. Waghé, Fabrication of Metal (Cu and Cr) Incorporated Nickel Oxide Films for Electrochemical Oxidation of Methanol, *Crystals* 11 (11) (2021), <https://doi.org/10.3390/crys11111398>.

[62] P.S. Murthy, V.P. Venugopalan, D.A. Das, S. Dhara, R. Pandiyar, A.K. Tyagi, In International Conference on Nanoscience, Engineering and Technology (ICONSET 2011). Antibiofilm Activity of Nano Sized CuO, IEEE, Chennai, 2011, pp. 580–583, <https://doi.org/10.1109/ICONSET.2011.6168037>.

[63] M.M. Lacerda, F. Kargar, E. Aytan, R. Samnakay, B. Debnath, J.X. Li, A. Khitun, R. K. Lake, J. Shi, A.A. Balandin, Variable-Temperature Inelastic Light Scattering Spectroscopy of Nickel Oxide: Disentangling Phonons and Magnons, *Appl. Phys. Lett.* 110 (20) (2017), 202406, <https://doi.org/10.1063/1.4983810>.

[64] G. Lucazeau, Effect of pressure and temperature on raman spectra of solids: anharmonicity, *J. Raman Spectrosc.* 34 (7–8) (2003) 478–496, <https://doi.org/10.1002/jrs.1027>.

[65] Y. Yang, Y. Li, Y. Jiang, M. Zheng, T. Hong, X. Wu, C. Xia, The Electrochemical Performance and CO<sub>2</sub> Reduction Mechanism on Strontium Doped Lanthanum Ferrite Fuel Electrode in Solid Oxide Electrolysis Cell, *Electrochim. Acta* 284 (2018) 159–167, <https://doi.org/10.1016/j.electacta.2018.07.187>.

[66] P.M. Albrecht, D. Jiang, D.R. Mullins, CO<sub>2</sub> adsorption as a flat-lying, tridentate carbonate on CeO<sub>2</sub>(100), *J. Phys. Chem. C* 118 (17) (2014) 9042–9050, <https://doi.org/10.1021/jp501201b>.

[67] Y. Zhou, A.J. Martín, F. Dattila, S. Xi, N. López, J. Pérez-Ramírez, B.S. Yeo, Long-chain hydrocarbons by CO<sub>2</sub> electroreduction using polarized nickel catalysts, *Nat. Catal.* 5 (6) (2022) ble, <https://doi.org/10.1038/s41929-022-00803-5>.